iScience

CellPress
OPEN ACCESS

Article

Large-scale voltage imaging in behaving mice using targeted illumination

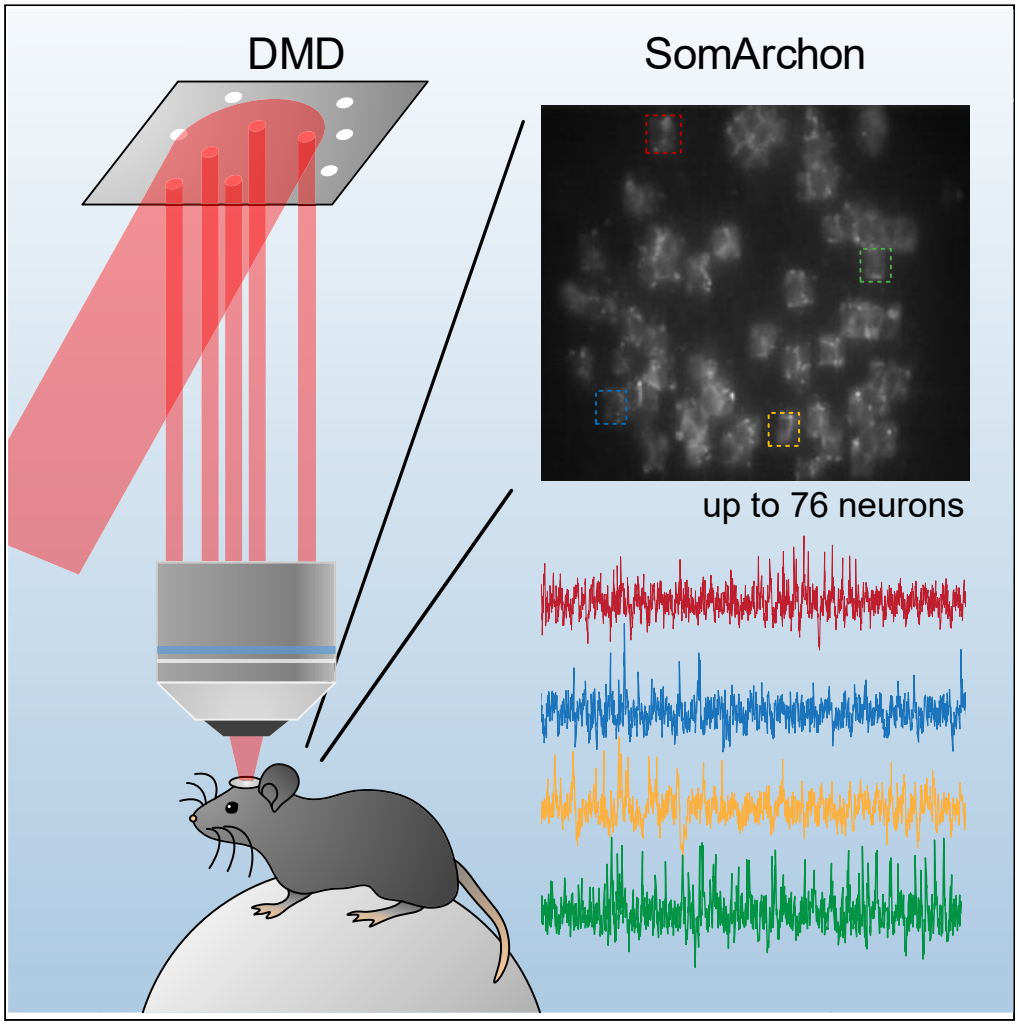

Sheng Xiao, Eric Lowet, Howard J. Gritton, ..., Edward S. Boyden, Jerome Mertz, Xue Han

xuehan@bu.edu

Highlights

An easily implementable digital-micromirror-based targeted illumination microscope

Targeted illumination improves voltage imaging signal contrast in the brain

Targeted illumination decreases photobleaching and reduces background in the brain

Routine voltage imaging of tens of neurons simultaneously in behaving mice

Xiao et al., iScience *24*, 103263
November 19, 2021
https://doi.org/10.1016/j.isci.2021.103263

iScience

CellPress
OPEN ACCESS

Article

Large-scale voltage imaging in behaving mice using targeted illumination

Sheng Xiao,[1,8] Eric Lowet,[1,8] Howard J. Gritton,[1,2,8] Pierre Fabris,[1] Yangyang Wang,[1] Jack Sherman,[1] Rebecca A. Mount,[1] Hua-an Tseng,[1] Heng-Ye Man,[3] Christoph Straub,[4] Kiryl D. Piatkevich,[5] Edward S. Boyden,[6,7] Jerome Mertz,[1] and Xue Han[1,9,*]

SUMMARY

Recent improvements in genetically encoded voltage indicators enabled optical imaging of action potentials and subthreshold transmembrane voltage *in vivo*. To perform high-speed voltage imaging of many neurons simultaneously over a large anatomical area, widefield microscopy remains an essential tool. However, the lack of optical sectioning makes widefield microscopy prone to background cross-contamination. We implemented a digital-micromirror-device-based targeted illumination strategy to restrict illumination to the cells of interest and quantified the resulting improvement both theoretically and experimentally with SomArchon expressing neurons. We found that targeted illumination increased SomArchon signal contrast, decreased photobleaching, and reduced background cross-contamination. With the use of a high-speed, large-area sCMOS camera, we routinely imaged tens of spiking neurons simultaneously over minutes in behaving mice. Thus, the targeted illumination strategy described here offers a simple solution for widefield voltage imaging of many neurons over a large field of view in behaving animals.

INTRODUCTION

Recent advances in genetically encoded voltage indicators (GEVIs) have enabled the direct measurement of transmembrane voltage changes from individual neurons in the mammalian brain (Abdelfattah et al., 2019; Adam et al., 2019; Fan et al., 2020; Gong et al., 2015; Piatkevich et al., 2019; Villette et al., 2019). In particular, a few newly developed GEVIs, including SomArchon, QuasAr3, Voltron, ASAP3, and Ace2N, have been shown to be able to capture individual action potentials in behaving mice. Of these high-performance GEVIs, several are fully genetically encoded, whereas others are hybrid, requiring exogenous chemicals (Bando et al., 2019; Beck et al., 2019; Kannan et al., 2019; Knöpfel and Song, 2019; Ma et al., 2019; Peng et al., 2017; Xu et al., 2017). One class of fully genetically encoded indicators utilizes fluorophores fused to voltage-sensitive protein domains derived from voltage-gated ion channels, voltage-sensitive phosphatases, or rhodopsins (Bando et al., 2019; Beck et al., 2019; Kannan et al., 2019; Knöpfel and Song, 2019; Peng et al., 2017; Xu et al., 2017). For these GEVIs, changes in transmembrane voltage induce confirmational transitions of the voltage sensitive domains, which subsequently alters the intensity of the tethered fluorophore or the efficiency of Förster resonance energy transfer involving the fluorophores. Another class of fully genetically encoded indicators is single compartment and detects the intrinsic voltage-dependent fluorescence of engineered rhodopsins, such as QuasAr3, Archon, and SomArchon (Adam et al., 2019; Piatkevich et al., 2018, 2019). To improve fluorescence signals, bright chemical fluorophores have also been explored in the design of GEVIs, yielding a class of high-performance hybrid GEVIs that requires both exogeneous chemical dyes and the corresponding voltage-sensing protein counterparts (Abdelfattah et al., 2019, 2020; Ma et al., 2019). With rapid and continued improvements of GEVIs, voltage imaging offers an exciting opportunity for direct analysis of neuronal voltage in the mammalian brain.

To optically capture fast transmembrane voltage fluctuations, especially action potentials that occur on the millisecond timescale, fluorescence voltage imaging requires a sampling rate of several hundred hertz or more. Point scanning techniques, such as multiphoton microscopy, produce minimal signal cross-contamination and out-of-focus background due to confined excitation volumes (Mertz, 2019) but are generally

[1]Department of Biomedical Engineering, Boston University, Boston, MA 02215, USA

[2]Department of Comparative Biosciences, University of Illinois, Urbana, IL 61802, USA

[3]Department of Biology, Boston University, Boston, MA 02215, USA

[4]Department of Biomedical Sciences, College of Osteopathic Medicine, University of New England, Biddeford, ME 04005, USA

[5]School of Life Sciences, Westlake University, Westlake Laboratory of Life Sciences and Biomedicine, Westlake Institute for Advanced Study, Hangzhou, Zhejiang, China

[6]MIT McGovern Institute for Brain Research, MIT, Cambridge, MA 02139, USA

[7]Howard Hughes Medical Institute, MIT, Cambridge, MA 02139, USA

[8]These authors contributed equally

[9]Lead contact

*Correspondence: xuehan@bu.edu

https://doi.org/10.1016/j.isci.2021.103263

limited to video-rate acquisition speeds as they rely on mechanical scanners. Fast random-access scanning using acousto-optic deflectors has been demonstrated with kilohertz sampling rates (Villette et al., 2019), although these devices require a complicated setup, are sensitive to motion artifacts, and have a limited field of view (FOV) of a few preselected cells. More recently, kilohertz frame rate two-photon imaging over an FOV of 50 × 250 μm^2 has been demonstrated by implementing passive pulse splitting from a specialized low-repetition rate laser (Wu et al., 2020). However, stringent alignment requirements, high cost, and lack of long-term system stability hinder its widespread application in neuroscience studies.

Widefield microscopy, especially when equipped with newly developed high-speed, large-area, and low-noise sCMOS cameras, remains a cost-effective and easily implementable solution for wide FOV, fast frame-rate imaging. This ability to image a large FOV at high spatiotemporal resolution is particularly critical to resolve morphological details of individual neurons, record multiple neurons, and correct for tissue movement associated with physiological processes (i.e., heart rate and breathing) that are unavoidable when imaging awake behaving animals. However, a major limitation of widefield microscopy is its inability to reject out-of-focus and scattered light (Mertz, 2011), making it prone to signal contamination and background shot noise caused by nonspecific fluorescence excitation (Harris et al., 2016). To address this problem molecularly, soma and proximal dendrite targeting motifs (Lim et al., 2000) have been used to reduce the expression of GEVIs throughout neuronal processes, such as in SomArchon, QuasAr3, Voltron, and ASAP3 (Abdelfattah et al., 2019; Adam et al., 2019; Fan et al., 2020; Piatkevich et al., 2019; Villette et al., 2019). Restricting the expression of GEVIs to a sparse subset of neurons can also help reduce background signal contamination *in vivo*, and this strategy was recently used to achieve simultaneous imaging of tens of cortical L1 neurons using the hybrid sensor Voltron (Abdelfattah et al., 2019).

Parallel to the molecular targeting of GEVIs, targeted illumination has also been developed to enhance image contrast and signal-to-noise ratio (SNR) (Adam et al., 2019; Fan et al., 2020; Xiao et al., 2018). By using a digital micromirror device (DMD) or a spatial light modulator to pattern the excitation light, targeted illumination confines fluorescent excitation to preselected areas of interest. Targeted illumination has been implemented in extended depth of field microscopy for video rate calcium imaging (Xiao et al., 2018) and was recently applied to voltage imaging *in vivo* in sparsely labelled tissue samples (Adam et al., 2019; Fan et al., 2020). However, the benefits of targeted illumination for voltage imaging have only been demonstrated on small scales of up to 5 neurons over a limited FOV. To quantitatively assess the improvement of targeted illumination, we first developed a theoretical model for widefield optical voltage imaging in brain tissue for targeted or widefield illumination. We then experimentally compared the effect of the two illumination conditions on SomArchon optical voltage signals by integrating a DMD-based targeted illumination module into a standard widefield microscope. We verified that targeted illumination reduced nonspecific background and fluorescence signal cross-contamination in the brain, leading to increased SomArchon spike signal-to-background ratio and reduced photobleaching. With such improvement, we demonstrated for the first time large-scale SomArchon voltage imaging from up to 76 neurons over an anatomical area of 360 × 180 μm^2 at 500 Hz in densely labelled neural tissue, while maintaining signal contrast over several continuous minutes. These results demonstrate that integrating a DMD-targeted illumination system into a standard widefield microscope represents a practical and easily implementable strategy for voltage imaging of many neurons simultaneously over a large FOV in behaving animals.

RESULTS

Computational modeling of the effects of targeted illumination on optical crosstalk in widefield optical imaging

Motivated by the unique advantage of widefield microscopy in performing optical voltage imaging with high spatiotemporal resolution over large FOVs, we considered the benefits of targeted illumination to enhance fluorescence signal quality. We first developed a theoretical model to estimate how targeted illumination reduces signal crosstalk originating from nearby neurons that are not actively being imaged. We modeled neurons as 15-μm diameter spherical shells and considered contributions from both out-of-focus fluorescence and tissue scattering by modeling light propagation through scattering media using the radiative transfer equation in the forward scattering limit (Ishimaru, 1999) (see STAR Methods and Figure S1). In our model, we characterized crosstalk values from non-targeted neurons at distance D_x laterally and D_z axially from a region-of-interest (ROI) under widefield versus targeted illumination conditions (Figures 1A, 1B, S2, S3, and S4). To estimate the effect of targeted illumination on fluorescence voltage signal

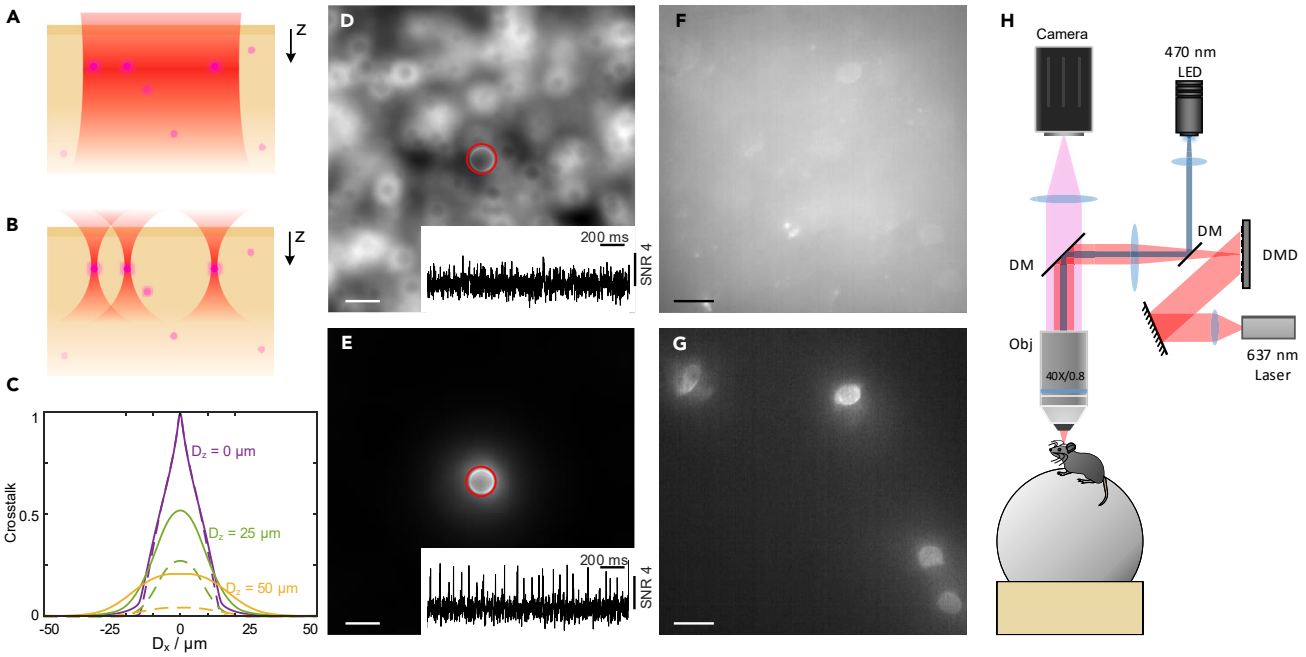

Figure 1. Theoretical models of the effect of targeted illumination on signal crosstalk in widefield optical imaging and a microscope design for experimental testing in awake mice

(A and B) Schematic of fluorescence imaging of individual neurons using widefield illumination (A) and targeted illumination (B). Purple dots illustrate the location of individual SomArchon expressing neurons. Red area illustrates the illumination beam for SomArchon excitation.

(C) Characterization of fluorescence crosstalk originating from a nontargeted neuron at lateral distance D_x and axial distance D_z from the neuron of interest under widefield and targeted illumination conditions. Solid lines, widefield illumination; dashed line, targeted illumination. Purple, $D_z = 0$ µm; green, $D_z = 25$ µm; yellow, $D_z = 50$ µm.

(D and E) Simulated fluorescence imaging of a single targeted neuron with background from multiple nontargeted neurons under widefield (D) and targeted (E) illumination. Illumination target is indicated by the red circle. Inserts, simulated fluorescence traces for the targeted neuron under widefield illumination (D) and targeted illumination (E).

(F–H) SomArchon voltage imaging in behaving mice. Example of SomArchon fluorescence images in the visual cortex of an awake head-fixed mouse voluntarily navigating a spherical treadmill (H), under widefield illumination (F) and targeted illumination (G). The same laser power density was used for the two illumination conditions, and 4 individual neurons were targeted in (G). DM, dichromatic mirror; Obj, objective lens. Scale bars, 20 µm.

quality, we further simulated membrane voltage using the Izhikevich-type integrate-and-fire neuron model (STAR Methods and Figure S5A) and converted the simulated membrane voltage traces into fluorescent traces (Figures 1D and 1E, inserts).

We found that in simulated fluorescence images, targeting illumination to a specific neuron (red circle: Figures 1D and 1E) substantially reduced the overall background in the imaging plane and therefore reduced the strength of crosstalk from neighboring neurons. In addition, the level of crosstalk contamination from a nonoverlapping axially displaced neuron is strongly affected by the distance between the out-of-focus neurons relative to the imaging plane (Figure 1C). In simulations featuring a larger number of out-of-focus neurons, targeted illumination was found to significantly improve spike signal-to-baseline ratio (SBR, detailed below) and spike detectability (Figures S6 and S7). These computational results confirm that, for widefield microscopy, targeting illumination only to neurons of interest can significantly improve fluorescence voltage signal quality by limiting signal contamination from neighboring out-of-focus neurons in brain tissue.

A simple, DMD-based targeted illumination-based widefield microscope for fast, large field-of-view voltage imaging

To experimentally evaluate the improvement of targeted illumination, we integrated a DMD into a custom-built widefield microscope configured for dual-color GFP and SomArchon imaging (Figure 1H). We performed voltage imaging of SomArchon expressing neurons, in cell cultures as well as in the visual cortex and hippocampus of awake head-fixed mice. Because SomArchon is fused to the GFP reporter, static

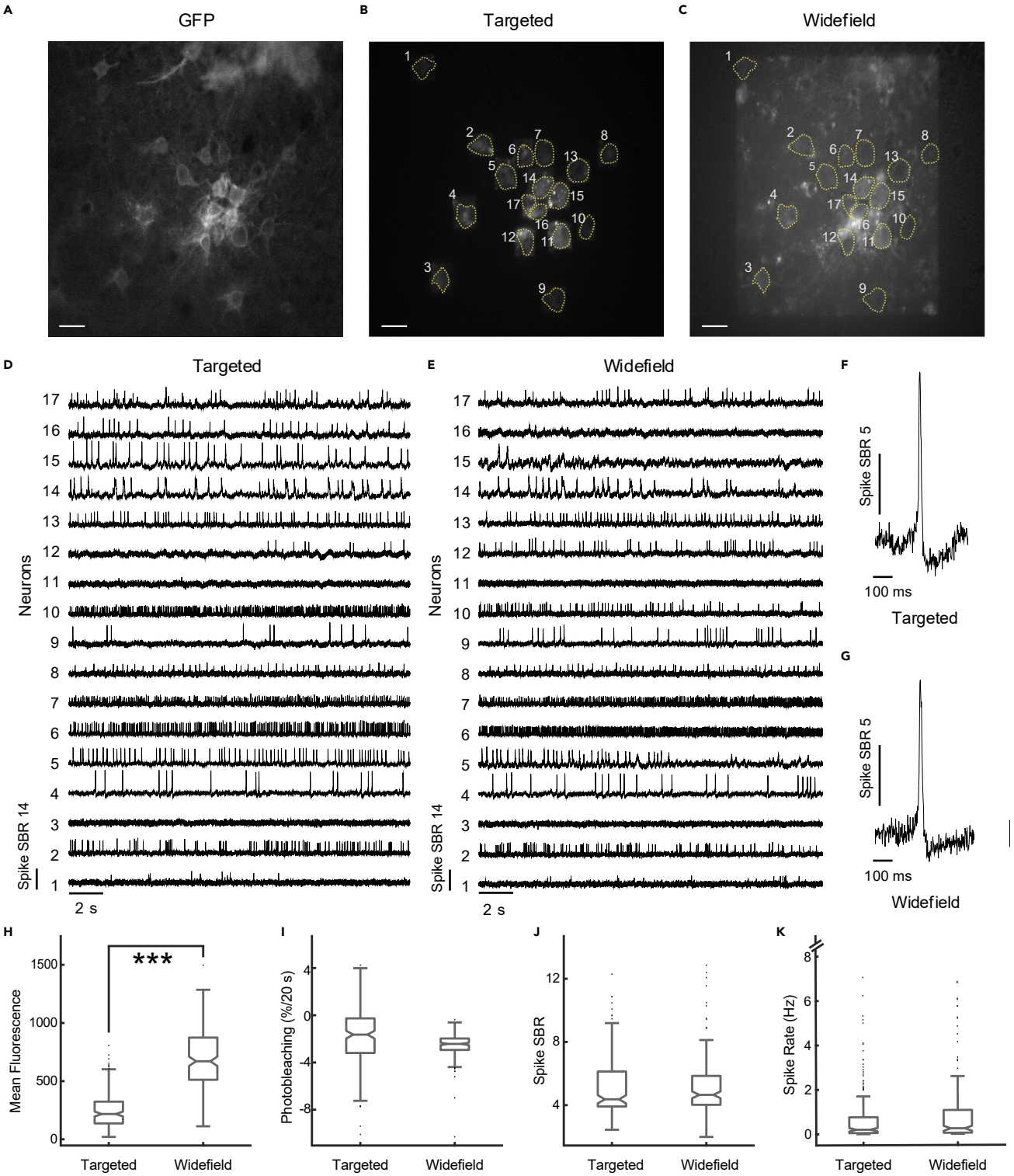

Figure 2. Targeted illumination minimally affects SomArchon imaging performance in cultured neurons

(A–C) An example FOV showing cultured neurons expressing SomArchon fused to a static GFP fluorophore; scale bars, 20 μm. (A) GFP fluorescence under widefield illumination. (B) SomArchon fluorescence under targeted illumination. (C) SomArchon fluorescence under widefield illumination.

(D and E) Example of SomArchon fluorescence traces from 17 simultaneously recorded neurons in the FOV illustrated in A, using targeted illumination (D) and widefield illumination (E).

Figure 2. *Continued*

(F and G) Example of individual spikes recorded from the same neuron with targeted illumination (F) and widefield illumination (G).

(H) Fluorescence values of individual ROIs recorded under widefield versus targeted illumination conditions in the same session (***, $p < 0.001$, zero is at the 100th percentile of the shuffled distribution).

(I) Photobleaching, calculated as the reduction of SomArchon fluorescence over 20-s periods. The illumination power density was ~2 W/mm^2 for both illumination conditions, for all recordings from cultured neurons.

(J) Spike SBR for targeted versus widefield illumination trials.

(K) Spike rate. Outliers greater than 8 Hz are not shown. All recordings were at 500 Hz frame rate. For all boxplots, the box indicates the median (middle line), 25th percentile (Q1, bottom line), and 75th percentile (Q3, top line), and the whiskers are Q1−1.5*(Q3-Q1) and Q3+1.5*(Q3-Q1). Outliers that exceed these values are shown as dots.

GFP reference images were first taken to identify SomArchon expressing neurons for targeted illumination. Consistent with what was observed in our computational models, we found that restricting illumination to the soma reduced the overall background fluorescence and accordingly enhanced the contrast of SomArchon fluorescence from individual cells in the brain (Figures 1F and 1G).

Targeted illumination exhibits minimal impact on SomArchon voltage imaging in cultured neurons with little out-of-focus background

We first examined whether targeted illumination improves SomArchon voltage imaging quality in cultured neurons. Cultured neurons on flat glass coverslips produce little out-of-focus fluorescence and therefore exhibit minimal signal contamination (Figure S2). To directly compare the effects of targeted versus widefield illumination on the same neurons, we imaged cultured neurons transduced with AAV9-syn-SomArchon-GFP that exhibit subthreshold membrane voltage (Vm) fluctuations and spontaneous action potentials. The same neurons were imaged with 20-s-long trials alternating between the two illumination conditions (n = 226 neurons recorded from 16 FOVs). Upon visual inspection, we noticed little difference in SomArchon fluorescence signal qualities under the two illumination conditions (Figures 2A–2G). We measured the mean fluorescence of each neuron, identified spikes, and calculated signal-to-baseline ratios (SBR) as detailed in STAR Methods and described later. To counterbalance targeted versus widefield illumination trials to avoid temporal biasing, we randomly selected two consecutive trials for each neuron, so that half of the neurons were imaged with targeted illumination first and the other half with widefield illumination first. We calculated the difference in mean fluorescence, spike SBR, and spike rate under the two conditions for each neuron in each random shuffle and performed the shuffling procedure 1,000 times. We compared the shuffled distribution with zero, the theoretical null hypothesis. One example shuffle representing the mean of the overall shuffled distribution is plotted in Figures 2H–2K.

We found that the ROI mean fluorescence under targeted illumination is significantly smaller than under widefield illumination ($p < 0.001$, zero is at 100th percentile of the shuffled distribution, outside of the 2.5–97.5 percentile of the shuffled distribution). We obtained a spike SBR of 5.1 $\pm$ 1.8 under targeted illumination (mean $\pm$ standard deviation, from 226 neurons in 16 FOVs, Figure 2I), similar to that under widefield illumination (5.1 $\pm$ 1.7, zero is at 45.7th percentile of the shuffled distribution, Figure 2I). Consequently, the spike rate was the same under the two conditions (0.8 $\pm$ 1.6 for targeted illumination and 1.1 $\pm$ 2.1 for widefield illumination, zero is at 47.5th percentile of the shuffled distribution, Figure 2J). Similarly, we obtained comparable SomArchon photobleaching rates under the two conditions, calculated as fluorescence reduction over 20-s recording periods (1.9 $\pm$ 2.4% for targeted illumination, 2.6 $\pm$ 1.2% for widefield illumination, zero is at 31.6th percentile of the shuffled distribution, Figures 2K and S9). We noticed a larger variation in photobleaching values under targeted illumination, likely due to the overall lower fluorescent values under targeted illumination (Figure 2H). Consistent with a lack of improvement of SomArchon voltage signals under targeted illumination, we found no difference in cross-correlations between neuron pairs, for both Vm and spikes between the two conditions (Figure S10). Together these results demonstrate that targeted illumination does not improve SomArchon voltage imaging performance in neuron cultures with minimal out-of-focus background.

Because SomArchon is sensitive enough to reveal changes in Vm (Piatkevich et al., 2019), the measured photon shot noise is mixed with underlying biological Vm fluctuations. Therefore, it is difficult to quantify the actual noise level to evaluate SomArchon signal qualities by calculating the absolute single-to-noise ratio (SNR). We thus calculated the spike SBR, defined as the amplitude of the spike divided by the standard deviation of the baseline voltage fluctuations (see STAR Methods). Because neurons have varying Vm fluctuations due to intrinsic differences in biophysical properties and synaptic connectivities, spike detection is

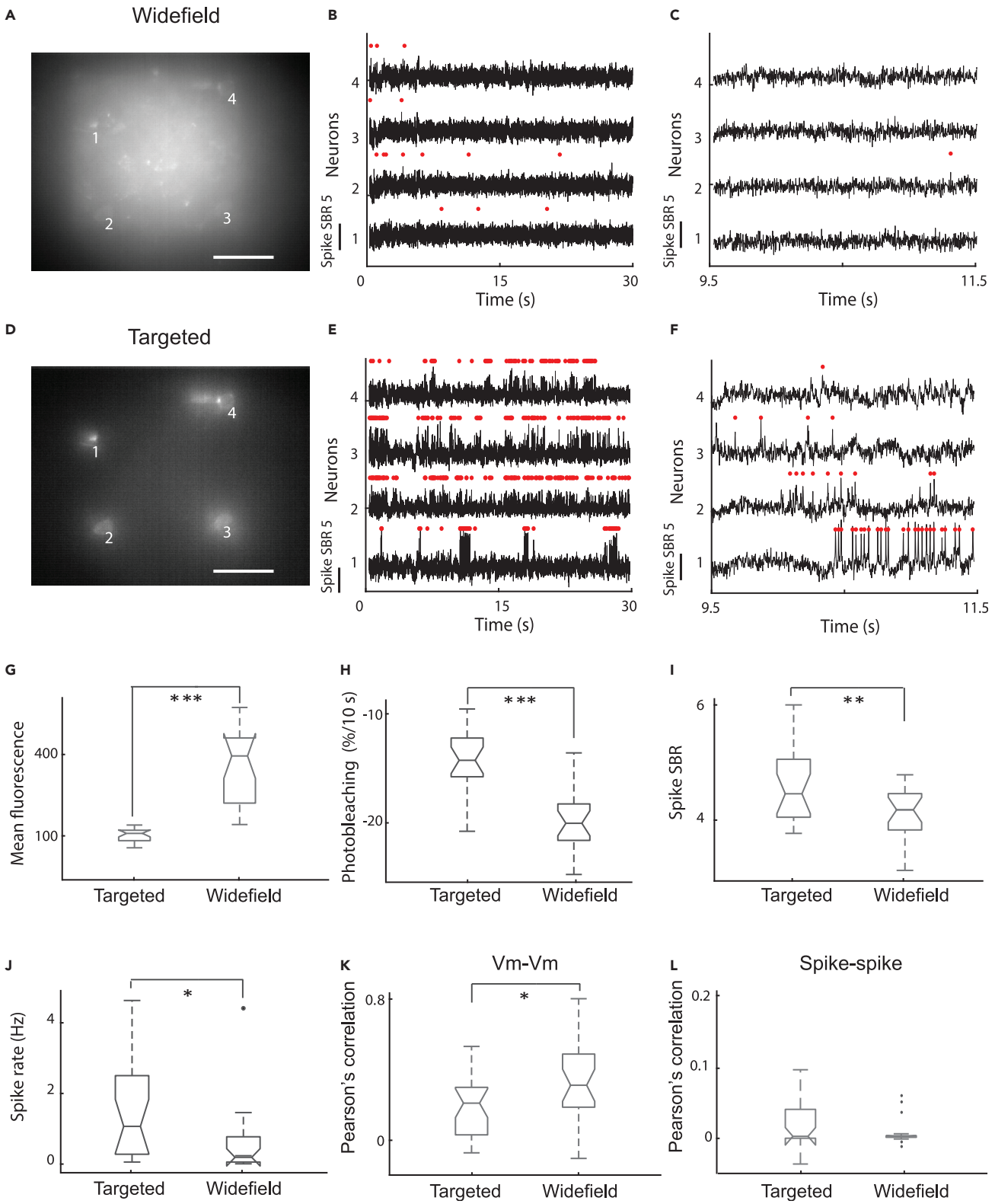

Figure 3. Targeted illumination improves SomArchon voltage imaging performance in the visual cortex of behaving mice

SomArchon expressing neurons in layers 1 and 2 of the visual cortex, 50–150 μm below the optical window, were imaged. GFP fluorescence was used for neuron localization.

Figure 3. *Continued*

(A–E) SomArchon voltage imaging under widefield illumination. (A) An example FOV showing SomArchon fluorescence averaged over the entire recording session. Scale bar, 50 μm. The excitation power density was 3 W/mm^2, corresponding to a total excitation power of 54 mW for the entire FOV in this imaging session. (B and C) Example SomArchon fluorescence traces (B), and zoom-in view (C), from simultaneously recorded 4 neurons indicated in (A), over a 10-s-long recording period.

(D–F) SomArchon voltage imaging under targeted illumination. The excitation power density was 3 W/mm^2, corresponding to a total excitation power of 3.4 mW across the 4 preselected ROIs in this imaging session. (D–F) Same as in (A–C) but for targeted illumination.

(G) Mean fluorescence values of individual ROIs recorded under widefield versus targeted illumination conditions (***, p = 1.73e^{-8}, paired t-test, df = 20).

(H) SomArchon photobleaching, calculated as fluorescence decay over 10 s for widefield versus targeted illumination conditions (***, p = 1.33e^{-10}, paired t-test, df = 20).

(I) Spike SBR for the two conditions (*, p = 0.003, paired t-test, df = 20).

(J) Spike rate for the two conditions (*, p = 0.016, paired t-test, df = 20).

(K) Vm-Vm correlations between simultaneously recorded neuron pairs with targeted versus widefield illumination (*, p = 0.024, paired t-test, df = 26).

(L) Spike-spike correlation between simultaneously recorded neuron pairs with targeted versus widefield illumination (p = 0.28, paired t-test, df = 26). For all boxplots, the box indicates the median (middle line), 25th percentile (Q1, bottom line), and 75th percentile (Q3, top line), and the whiskers are Q1−1.5*(Q3-Q1) and Q3+1.5*(Q3-Q1). Outliers that exceed these values are shown as dots.

thus impacted by spontaneous Vm variations in individual neurons. To evaluate our spike detection and SBR calculation algorithms, we simulated membrane voltage using the Izhikevich-type integrate-and-fire neuron model that takes into account both action potentials and biological Vm (Figure S5A). In addition, to model experimentally measured noise signals, we added different levels of Gaussian white noise (Figures S5B, S5D, S5E). We calculated the theoretical SBR as the spike amplitude divided by the experimentally measurable baseline fluctuations that contain both the biological Vm signals and the white noise and the theoretical SNR as the spike amplitude divided by the standard deviation of the white noise only. We found that our SBR estimation underestimated the theoretical SNR, but it better reflected the theoretical SBR that includes biological Vm variations (Figure S5C). Thus, although our spike SBR measure is an underestimation of SomArchon molecular performance, it provides an intuitive and spike-insensitive measure of the optical voltage signal quality, especially for *in vivo* recordings where conditions can vary substantially between imaging sessions. To further evaluate how varying image acquisition rates impact spike detection, we compared the percentage of spikes detected using SomArchon fluorescence traces with the ground truth spikes identified in simultaneous patch clamp recordings in brain slices. Interestingly, at 500 Hz, we detected significantly more spikes than at 1,000 Hz (Figure S11), consistent with what was observed previously with voltage sensitive dyes (Quicke et al., 2019), as a lower sampling rate can provide better SBR by accumulating more photons per image frame.

Targeted illumination improves SomArchon spike SBR, reduces fluorescence crosstalk in the visual cortex of awake mice

To quantify the effect of targeted illumination in the brain, visual cortex neurons were transduced with AAV9-syn-SomArchon-GFP. We imaged SomArchon expressing neurons 50–150 μm below the optical window positioned above the pia mater, corresponding to layers 1 and 2, when mice were head-fixed and freely locomoting on a spherical treadmill. For each FOV, we alternated 10-s-long voltage imaging sessions randomly between targeted illumination and widefield illumination conditions. We kept the ballistic excitation power density constant for the same FOV when imaged under the two illumination conditions, 3–5 W/mm^2 across all FOVs imaged, corresponding to 0.7–1.1 mW per neuron (assuming a 15 × 15 μm^2 square excitation region). However, for *in vivo* imaging, the actual excitation power is further affected by tissue scattering. Photons targeting a cell can be scattered away from the ROI, whereas photons targeting non-ROI regions can eventually reach the ROI due to backward scattering. Therefore, although the same excitation power density was applied in both conditions, neurons under widefield illumination conditions can actually be exposed to higher excitation power, leading to faster photobleaching. Indeed, we found that targeted illumination significantly reduced the photobleaching of SomArchon fluorescence, exhibiting a fluorescence decay of 14.95 ± 3.2% over 10 s for targeted illumination versus 20.38 ± 3.05% for widefield illumination (p = 1.33e^{-10}, paired t-test, df = 20, Figure 3H). Furthermore, we found that SomArchon fluorescence was significantly higher under widefield conditions than targeted illumination conditions, confirming a reduction of fluorescence background by targeted illumination (p = 1.73e^{-8}, paired t-test, df = 20, Figure 3G).

We further identified spikes and calculated SBRs. Targeted illumination resulted in a significant increase in SomArchon spike SBR, achieving 4.6 ± 0.6, significantly higher than the 4.1 ± 0.43 obtained with widefield

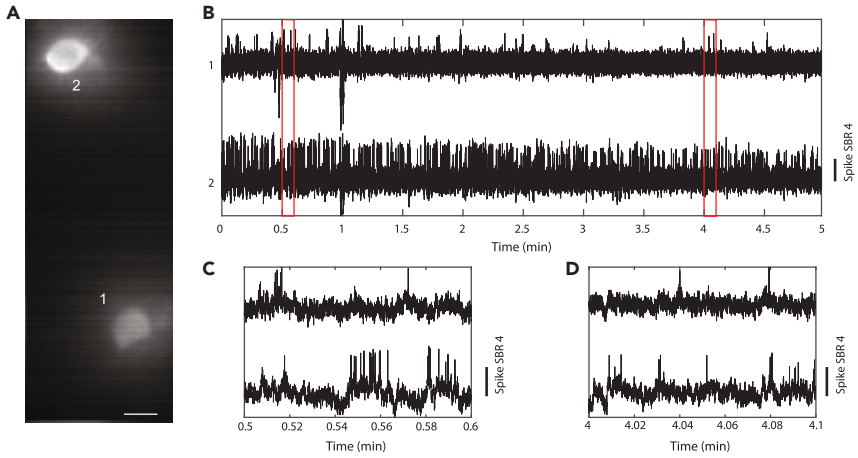

Figure 4. An example of 5-min-long continuous recording from two visual cortex neurons

(A) SomArchon fluorescence image from two neurons imaged with targeted illumination. Scale bar, 10 μm.

(B) SomArchon fluorescence traces throughout the entire 5-min-long recording session.

(C and D) Zoom-in view of SomArchon fluorescence toward the beginning (C) and the end of the recording session (D).

illumination ($p = 0.003$, paired t-test, df = 20 neurons, Figure 3I). This improvement in spike SBR accordingly led to a greater frequency of spikes being identified under targeted illumination, because spikes can be better separated from baseline Vm fluctuations (Figures 3J and S7B). To examine how targeted illumination impacts correlation measurements between simultaneously recorded neuron pairs, we computed spike-spike and Vm-Vm correlations. We observed that targeted illumination significantly reduced Vm-Vm correlation values (Figure 3K). However, spike-spike correlation values remained largely constant under both conditions (Figure 3L). Because spikes are only produced when Vm depolarization reaches sodium channel activation threshold for action potential generation, joint synaptic inputs that produce correlative low-amplitude subthreshold Vm changes between neuron pairs will not be captured by spike-spike correlation measures. The fact that Vm-Vm correlation, but not spike-spike correlation, is reduced by targeted illumination highlights that Vm signals contain a higher proportion of background signal crosstalk than spike signals.

With targeted illumination, the drastically reduced background fluorescence and consequently enhanced spike SBR allowed us to reduce laser excitation intensity during voltage imaging. This reduction of overall ballistic illumination intensity and the reduction of ROI exposure to backscattered light help alleviate SomArchon photobleaching and thus enabled longer recording sessions with targeted illumination. Figure 4 represents an example of a continuous recording of 5 min, revealing that excellent spike SBRs can be maintained throughout the recording duration. Of the two simultaneously recorded neurons, the spike SBR for neuron 1 was 4.13 ± 1.1 (mean $\pm$ standard deviation, n = 1,366 spikes) and for neuron 2 was 4.81 ± 1.29 (mean $\pm$ standard deviation, n = 261 spikes). However, we did notice a reduction in spike SBR over time ($p = 9e^{-14}$, Kruskal-Wallis, df = 1,626 spikes, from 2 neurons combined), which reflects the effect of fluorescence photobleaching.

Targeted illumination allows for large-scale recordings from dozens of CA1 neurons simultaneously in awake mice

Having established the advantages of targeted illumination, we deployed targeted illumination for simultaneous recording of many neurons in the dorsal hippocampus CA1 region that has a densely populated pyramidal cell layer. We sampled FOVs of 360×180 μm^2, often containing tens of easily identifiable SomArchon expressing neurons. We performed 6 recordings of 17 or more CA1 neurons (37 ± 22 neurons per session, mean $\pm$ standard deviation), while mice were head-fixed and navigating on a spherical treadmill. We identified spiking neurons based on the automatic spike detection algorithm and visual inspection as detailed in STAR Methods (Figure S5). Across these recording sessions, we recorded a total of 222 spiking neurons, with a spike SBR of 4.16 ± 0.5 (mean $\pm$ standard deviation, n = 222 spiking neurons, Figures 5, S12). In one recording, we were able to record 76 neurons simultaneously in a densely labelled area, and detected spikes in 48 of those neurons, over a 90-s-long recording period (Figures 5 and S13). The mean spike SBR of these neurons was 4.53 ± 0.38 (mean $\pm$ standard deviation, n = 48 neurons).

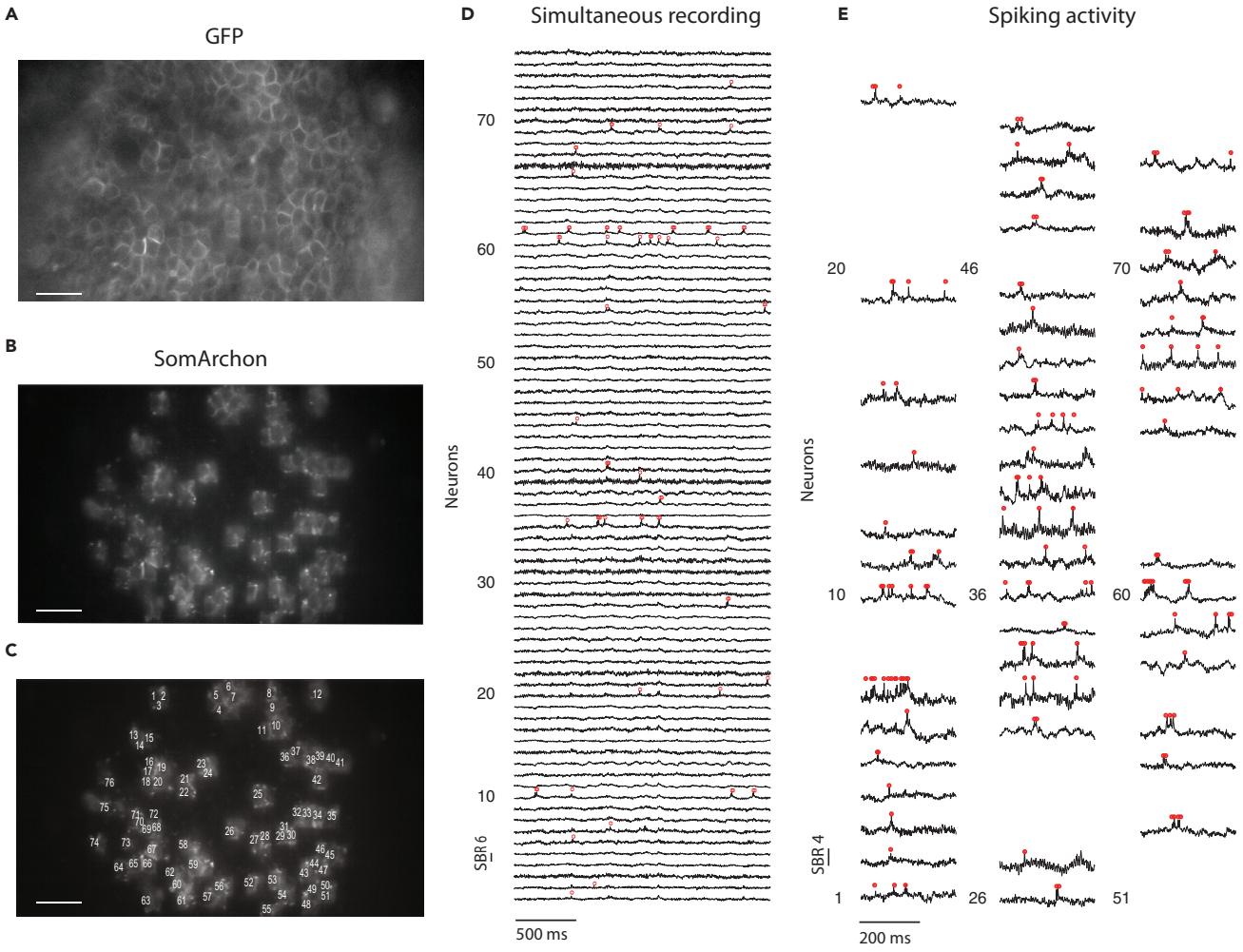

Figure 5. An example large-scale simultaneous recording of 76 CA1 neurons using targeted illumination in a behaving mouse

(A–C) SomArchon expressing CA1 neurons in the FOV, visualized with GFP fluorescence (A), SomArchon fluorescence imaged with targeted illumination (B) and with each neuron labelled (C). Scale bars, 50 μm.

(D) Example traces from 76 simultaneously recorded CA1 neurons. 2.5-s recordings are shown here. Identified spikes are marked by red dots.

(E) Zoom-in view of periods with identified spikes in the 48 spiking neurons. The illumination power density was ~4.5 W/mm^2 for this and all other CA1 recordings.

DISCUSSION

Widefield microscopy remains an important imaging technique for high-speed voltage imaging of many neurons simultaneously within a large FOV in task-performing animals. To improve optical sectioning of widefield fluorescence microscopy we integrated a standard DMD-based targeted illumination system into a widefield microscope equipped with a high-speed, large-FOV sCMOS camera. We estimated the impact of targeted illumination on voltage imaging theoretically, and then experimentally quantified the improvement of targeted illumination for SomArchon voltage imaging in the brains of behaving mice and in neuron cultures. We found that by restricting illumination to neuronal cell bodies, we were able to significantly improve SomArchon performance in the brain by reducing out-of-focus background fluorescence and therefore increasing SomArchon signal contrast, although not in neuron cultures with little out-of-focus background. This improvement in the case of brain imaging led to increased spike SBR and reduced SomArchon photobleaching. With such improvements in SomArchon signal quality, together with a high-speed large sensor size sCMOS camera, we were able to record optical voltage signals from over 70 neurons simultaneously over a wide FOV of 360 × 180 μm^2 at 500 Hz in the densely labelled CA1 pyramidal cell layer in behaving mice.

In addition to large-scale and long-term imaging, our DMD-based targeted illumination widefield microscope presents several other advantages that help facilitate its use in general voltage imaging applications. With SomArchon, only a single-color excitation source is required to be patterned with the DMD; this greatly simplified our targeted illumination module in that the DMD can be directly projected onto the sample through a tube lens and an objective, as opposed to alternative systems that involve dual-color excitation (Adam et al., 2019) or more complicated holographic targeting (Fan et al., 2020). For wide FOV SomArchon voltage imaging, large area excitation with a power density on the order of a few W/mm^2 is necessary. Although typical LEDs provide insufficient power density, this power density can be easily attained with a multimode laser diode array because of the widefield nature of our DMD-based targeting strategy. Such a light source is also free of the undesirable speckle noise associated with targeting techniques that require coherent sources that are particularly sensitive to animal motion (Fan et al., 2020). Moreover, in our system, the initial GFP reference imaging was performed using the same widefield microscope with the simple addition of blue LED excitation. Such an integrated widefield microscope system provides a significantly less costly and less complicated method of obtaining reference images than an alternative method involving a separate two-photon microscope (Adam et al., 2019; Fan et al., 2020). Because both GFP and SomArchon fluorescence are captured by the same camera, both images are automatically co-registered, further sidestepping the issue of image registration and long-term system stability across multiple microscope modules.

Single-cell level imaging in living animals can be affected by tissue motion due to metabolic, physiological, and vascular changes, which in principle can be corrected offline by image registration (Mohammed et al., 2016; Pnevmatikakis and Giovannucci, 2017). Targeting illumination only to cell membranes using holographic projections, however, is sensitive to translational movement due to the restricted area of illumination, which introduces additional challenges when preparing animal subjects and designing behavioral tasks. The DMD-based widefield targeting strategy described here makes allowances for such registration by adjusting ROI window sizes to accommodate for such tissue motion. For example, increasing the region of targeted illumination to capture the morphological details of a neuron allows small translational movements to be effectively corrected offline after image acquisition. Single-photon widefield imaging is also more robust to axial movements owing to its lack of optical sectioning (Mertz, 2011), which enables continuous signal recording even in the event of small axial fluctuations. This advantage is retained to a large degree when performing DMD-based targeted illumination as described here, in comparison to the use of holographic projections (Fan et al., 2020). Techniques with confined excitation volume limited to narrow z-axis profiles, such as two-photon microscopy (Helmchen and Denk, 2005), are also highly sensitive to image motion expected from behaving animals (Griffiths et al., 2020).

With regard to crosstalk reduction, a number of computational techniques have been developed over the past several years for cell identification and signal unmixing (Pnevmatikakis et al., 2016; Xie et al., 2021). These techniques generally rely on known signal models and can efficiently extract individual cell activities from out-of-focus background and neighboring crosstalk. The advantage of such approaches is that they are purely numerical and require no modification of the imaging setup. In contrast, our targeted illumination system applies a more physical approach to reduce out-of-focus background and crosstalk. The signals recorded with targeted illumination intrinsically exhibit higher SNR and thus benefit from reduced total excitation power and less photobleaching. However, an inconvenience of targeted illumination is that it requires a precalibration step involving the acquisition of a reference image, which may require the presence of a static label (GFP in our case), if the SomArchon fluorescence is inadequate. We note that the computational approaches and our targeted illumination approach are not mutually exclusive: they can potentially be combined for even larger scale high-fidelity neuronal voltage signal analysis.

An important advantage of using targeted illumination is the reduction of overall excitation power density arising from both direct ballistic excitation and indirect excitation from tissue backscattering. Indeed, we found that with the same incident illumination power, the neurons imaged under targeted illumination were exposed to lower net excitation power and therefore reduced photobleaching. This reduction in photobleaching is significant when performing brain imaging but less so when performing neuronal culture imaging with little out-of-focus background. Ultimately, the reduced background and consequently improved spike SBR allowed us to reduce the incident illumination power. As a result, we were able to perform continuous recordings over several minutes in duration, with only moderate reductions in spike SBR. This corresponds to hundreds of multi-second trials commonly used in system neuroscience

experimental designs. Although the performance of fluorescence-based activity indicators is always limited by photobleaching, the deployment of trial-based study designs where the excitation is turned off during inter-trial-intervals would enable voltage imaging over many trials and potentially over a greater cumulative duration than demonstrated here using continuous illumination.

To evaluate SomArchon signal quality, we calculated spike SBR. The baseline used in this SBR calculation contained both biological subthreshold membrane voltage fluctuations and intrinsic fluorescence shot noise. Neurons in intact neural circuits, especially in the awake brain, receive heterogenous synaptic inputs and exhibit distinct membrane biophysical properties, which lead to subthreshold membrane voltage fluctuations that are difficult to estimate. Thus, by itself, spike SBR estimation for each neuron cannot fully capture the quality of SomArchon signal contrast and represents an underestimate of SomArchon performance as confirmed by our spiking neuron models. However, spike SBRs of the same neuron when compared under the two illumination conditions can provide a quantitative measure of the fluorescence signal quality, providing direct experimental evidence that targeted illumination significantly improves the quality of SomArchon voltage imaging. Because spike SBR is a key consideration for spike detection, the fact that we detected more spikes under targeted illumination condition further demonstrates the improvement of SomArchon voltage signal quality.

Limitations of the study

A drawback of using larger ROIs to accommodate tissue motion, however, is the increased excitation power. To avoid tissue heating, the total excitation power ideally needs to be kept as low as possible. In our experiments, we used an excitation power of 0.7–1.1 mW per neuron. The maximum number of neurons imaged is thus estimated to be 90–140, if we are to keep the total excitation power under 100 mW as recently suggested to maintain tissue temperature below 37°C (Adam et al., 2019). But when larger ROIs (and hence higher excitation power per ROI) are used to accommodate larger tissue motion, the number of simultaneously imaged neurons should be reduced accordingly. In addition, in densely labelled regions such as hippocampus CA1, one might not be able to image every cell simultaneously within the FOV. Our simulation showed that it is beneficial to keep imaged cells separated by about 40 μm to minimize crosstalk (Figure S8). Therefore, in practice, we generally kept the number of imaged cells to be within the power limit, while maximizing the distances between neurons within the FOV. This typically resulted in checkerboard-like illumination patterns similar to Figure 5.

STAR★METHODS

Detailed methods are provided in the online version of this paper and include the following:

- KEY RESOURCES TABLE
- RESOURCE AVAILABILITY
  - Lead contact
  - Materials availability
  - Data and code availability
- EXPERIMENTAL MODEL AND SUBJECT DETAILS
  - Primary neuron cultures
  - Animals
  - Brain slices
- METHOD DETAILS
  - Simulated data theory for widefield fluorescence imaging
  - Crosstalk simulation under different illumination conditions
  - Membrane voltage simulation
  - Simulation of imaging neuronal voltage dynamics under different illumination conditions
  - Custom widefield optical imaging setup
- QUANTIFICATION AND STATISTICAL ANALYSIS
  - Data analysis
  - Neuron ROI selection and signal analysis
  - SomArchon photobleaching estimation
  - Spike detection and spike SBR calculation
  - Pearson correlation analysis
  - Statistical analysis

SUPPLEMENTAL INFORMATION

Supplemental information can be found online at https://doi.org/10.1016/j.isci.2021.103263.

ACKNOWLEDGMENTS

X.H. acknowledges funding from NIH (1R01MH122971, 1R01NS115797, R01NS109794, 1R34NS111742), NSF (CBET-1848029, DIOS-2002971). J.M. and X.H. acknowledges funding from NIH (R01EB029171), and E.L. acknowledges funding from Boston University Center for Systems Neuroscience. J.S. is supported by a training grant from NIH (5T32GM008541-23). The funders had no role in study design, data collection and analysis, decision to publish, or preparation of the manuscript. We thank members of the Han Lab for technical support, and Dr. Bernardo Sabatini for providing resources for simultaneous SomArchon voltage imaging and electrophysiology experiments in brain slices.

AUTHOR CONTRIBUTIONS

S.X., E.L., H.J.G, and J.S. performed imagine experiments in cultured neurons and in the brains of awake mice. S.X. and E.L. performed computational simulations. E.L., P.F., H.T. and Y.W. analyzed the data. R.A.M. and E.L. prepared animals for the experiments. H.M. provided cultured neurons. C.S., K.D.P. and E.S.B. conducted simultaneous voltage imaging and electrophysiology experiments in brain slices. J.M. consulted on imaging system design. X.H. supervised the study. S.X, E.L., H.J.G, and X.H. wrote the manuscript. All authors edited the manuscript.

DECLARATION OF INTERESTS

The authors declare no competing interests.

Received: April 19, 2021
Revised: August 30, 2021
Accepted: October 11, 2021
Published: November 19, 2021

REFERENCES

Abdelfattah, A.S., Kawashima, T., Singh, A., Novak, O., Liu, H., Shuai, Y., Huang, Y.C., Campagnola, L., Seeman, S.C., Yu, J., et al. (2019). Bright and photostable chemigenetic indicators for extended in vivo voltage imaging. Science *365*, 699–704. https://doi.org/10.1126/science.aav6416.

Abdelfattah, A.S., Valenti, R., Zheng, J., Wong, A., Chuong, A.S., Hasseman, J.P., Jayaraman, V., Kolb, I., Korff, W., Lavis, L.D., et al. (2020). A general approach to engineer positive-going eFRET voltage indicators. Nat. Commun. *11*, 1–8. https://doi.org/10.1038/s41467-020-17322-1.

Adam, Y., Kim, J.J., Lou, S., Zhao, Y., Xie, M.E., Brinks, D., Wu, H., Mostajo-Radji, M.A., Kheifets, S., Parot, V., et al. (2019). Voltage imaging and optogenetics reveal behaviour-dependent changes in hippocampal dynamics. Nature *569*, 413–417. https://doi.org/10.1038/s41586-019-1166-7.

Bando, Y., Grimm, C., Cornejo, V.H., and Yuste, R. (2019). Genetic voltage indicators. BMC Biol. *17*, 1–12. https://doi.org/10.1186/s12915-019-0682-0.

Beck, C., Zhang, D., and Gong, Y. (2019). Enhanced genetically encoded voltage indicators advance their applications in neuroscience. Curr. Opin. Biomed. *12*, 111–117. https://doi.org/10.1016/j.cobme.2019.10.010.

Fan, L.Z., Kheifets, S., Böhm, U.L., Wu, H., Piatkevich, K.D., Xie, M.E., Parot, V., Ha, Y., Evans, K.E., Boyden, E.S., et al. (2020). All-optical electrophysiology reveals the role of lateral inhibition in sensory processing in cortical layer 1. Cell *180*, 512–535. https://doi.org/10.1016/j.cell.2020.01.001.

Gong, Y., Huang, C., Li, J.Z., Grewe, B.F., Zhang, Y., Eismann, S., and Schnitzer, M.J. (2015). High-speed recording of neural spikes in awake mice and flies with a fluorescent voltage sensor. Science *350*, 1361–1366. https://doi.org/10.1126/science.aab0810.

Griffiths, V.A., Valera, A.M., Lau, J.Y., Roš, H., Younts, T.J., Marin, B., Baragli, C., Coyle, D., Evans, G.J., Konstantinou, G., et al. (2020). Real-time 3D movement correction for two-photon imaging in behaving animals. Nat. Methods *17*, 741–748. https://doi.org/10.1038/s41592-020-0851-7.

Harris, K.D., Quiroga, R.Q., Freeman, J., and Smith, S.L. (2016). Improving data quality in neuronal population recordings. Nat. Neurosci. *19*, 1165–1174. https://doi.org/10.1038/nn.4365.

Helmchen, F., and Denk, W. (2005). Deep tissue two-photon microscopy. Nat. Methods *2*, 932–940. https://doi.org/10.1038/nmeth818.

Ishimaru, A. (1999). Wave Propagation and Scattering in Random Media (Academic Press).

Izhikevich, E.M. (2003). Simple model of spiking neurons. IEEE Trans. Neural Netw. *14*, 1569–1572. https://doi.org/10.1109/TNN.2003.820440.

Jacques, S.L. (2013). Optical properties of biological tissues: a review. Phys. Med. Biol. *58*, R37. https://doi.org/10.1088/0031-9155/58/11/R37.

Kannan, M., Vasan, G., and Pieribone, V.A. (2019). Optimizing strategies for developing genetically encoded voltage indicators. Front. Cell. Neurosci. *13*, 53. https://doi.org/10.3389/fncel.2019.00053.

Knöpfel, T., and Song, C. (2019). Optical voltage imaging in neurons: moving from technology development to practical tool. Nat. Rev. Neurosci. *20*, 719–727. https://doi.org/10.1038/s41583-019-0231-4.

Lim, S.T., Antonucci, D.E., Scannevin, R.H., and Trimmer, J.S. (2000). A novel targeting signal for proximal clustering of the Kv2.1 K+ channel in hippocampal neurons. Neuron *25*, 385–397. https://doi.org/10.1016/S0896-6273(00)80902-2.

Ma, Y., Bayguinov, P.O., and Jackson, M.B. (2019). Optical studies of action potential dynamics with hVOS probes. Curr. Opin. Biomed. *12*, 51–58. https://doi.org/10.1016/j.cobme.2019.09.007.

Mertz, J. (2019). Introduction to Optical Microscopy (Cambridge University Press).

Mertz, J. (2011). Optical sectioning microscopy with planar or structured illumination. Nat. Methods *8*, 811–819. https://doi.org/10.1038/nmeth.1709.

Mohammed, A.I., Gritton, H.J., Tseng, H.A., Bucklin, M.E., Yao, Z., and Han, X. (2016). An integrative approach for analyzing hundreds of neurons in task performing mice using wide-field calcium imaging. Sci. Rep. *6*, 1–16. https://doi.org/10.1038/srep20986.

Peng, L., Xu, Y., and Zou, P. (2017). Genetically-encoded voltage indicators. Chin. Chem. Lett. *28*, 1925–1928. https://doi.org/10.1016/j.cclet.2017.09.037.

Piatkevich, K.D., Bensussen, S., Tseng, H., Shroff, S.N., Lopez-Huerta, V.G., Park, D., Jung, E.E., Shemesh, O.A., Straub, C., Gritton, H.J., et al. (2019). Population imaging of neural activity in awake behaving mice. Nature *574*, 413–417. https://doi.org/10.1038/s41586-019-1641-1.

Piatkevich, K.D., Jung, E.E., Straub, C., Linghu, C., Park, D., Suk, H.J., Hochbaum, D.R., Goodwin, D., Pnevmatikakis, E., Pak, N., et al. (2018). A robotic multidimensional directed evolution approach applied to fluorescent voltage reporters article. Nat. Chem. Biol. *14*, 352–360. https://doi.org/10.1038/s41589-018-0004-9.

Pnevmatikakis, E.A., and Giovannucci, A. (2017). NoRMCorre: an online algorithm for piecewise rigid motion correction of calcium imaging data. J. Neurosci. Methods *291*, 83–94. https://doi.org/10.1016/j.jneumeth.2017.07.031.

Pnevmatikakis, E.A., Soudry, D., Gao, Y., Machado, T.A., Merel, J., Pfau, D., Reardon, T., Mu, Y., Lacefield, C., Yang, W., et al. (2016). Simultaneous denoising, deconvolution, and demixing of calcium imaging data. Neuron *89*, 285–299. https://doi.org/10.1016/j.neuron.2015.11.037.

Quicke, P., Song, C., McKimm, E.J., Milosevic, M.M., Howe, C.L., Neil, M., Schultz, S.R., Antic, S.D., Foust, A.J., and Knöpfel, T. (2019). Single-neuron level one-photon voltage imaging with sparsely targeted genetically encoded voltage indicators. Front. Cell. Neurosci. *13*, 39. https://doi.org/10.3389/fncel.2019.00039.

Stokseth, P.A. (1969). Properties of a defocused optical system. J. Opt. Soc. Am. *59*, 1314–1321. https://doi.org/10.1364/josa.59.001314.

Villette, V., Chavarha, M., Dimov, I.K., Bradley, J., Pradhan, L., Mathieu, B., Evans, S.W., Chamberland, S., Shi, D., Yang, R., et al. (2019). Ultrafast two-photon imaging of a high-gain voltage indicator in awake behaving mice. Cell *179*, 1590–1608. https://doi.org/10.1016/j.cell.2019.11.004.

Wu, J., Liang, Y., Chen, S., Hsu, C.L., Chavarha, M., Evans, S.W., Shi, D., Lin, M.Z., Tsia, K.K., and Ji, N. (2020). Kilohertz two-photon fluorescence microscopy imaging of neural activity in vivo. Nat. Methods *17*, 287–290. https://doi.org/10.1038/s41592-020-0762-7.

Xiao, S., Tseng, H.A., Gritton, H., Han, X., and Mertz, J. (2018). Video-rate volumetric neuronal imaging using 3D targeted illumination. Sci. Rep. *8*, 1–10. https://doi.org/10.1038/s41598-018-26240-8.

Xie, M.E., Adam, Y., Fan, L.Z., Böhm, U.L., Kinsella, I., Zhou, D., Rozsa, M., Singh, A., Svoboda, K., Paninski, L., and Cohen, A.E. (2021). High-fidelity estimates of spikes and subthreshold waveforms from 1-photon voltage imaging in vivo. Cell Rep. *35*, 108954. https://doi.org/10.1016/j.celrep.2021.108954.

Xu, Y., Zou, P., and Cohen, A.E. (2017). Voltage imaging with genetically encoded indicators. Curr. Opin. Chem. Biol. *39*, 1–10. https://doi.org/10.1016/j.cbpa.2017.04.005.

Yaroslavsky, A.N., Schulze, P.C., Yaroslavsky, I.v., Schober, R., Ulrich, F., and Schwarzmaier, H.J. (2002). Optical properties of selected native and coagulated human brain tissues in vitro in the visible and near infrared spectral range. Phys. Med. Biol. *47*, 2059. https://doi.org/10.1088/0031-9155/47/12/305.

STAR★METHODS

KEY RESOURCES TABLE

REAGENT or RESOURCE	SOURCE	IDENTIFIER
Bacterial and virus strains		
AAV-Syn-SomArchon 5.9×10^{-12} genome copies (GC)/ml	Addgene	RRID:Addgene_126941
Chemicals, peptides, and recombinant proteins		
DMEM/F12	Gibco	cat. # 21331020
Fetal Bovine Serum	R&D systems	cat. # S11150
Horse Serum, heat inactivated	Thermo Fisher Scientific	cat. # 26050070
Penicillin-Streptomycin	Thermo Fisher Scientific	cat. # 15140122
L-Cysteine hydrochloride	Millipore Sigma	cat. # C1276
L-Glutamine	Thermo Fisher Scientific	cat. # 35050061
Neurobasal Medium	Gibco	cat. # 21103049
NeuroCult SM1 Neuronal Supplement	Stemcell Technologies	cat. # 05711
5-fluoro-2-deoxyuridine	Millipore Sigma	cat. # 343333
Other		
Primary neuron cultures prepared from CD® (Sprague Dawley) IGS rat embryos	Charles River Laboratories	RRID:RGD_734476
Experimental models: organisms/strains		
Mouse: C57BL/6	Charles River Laboratories	RRID:MGI:5656552
Software and algorithms		
Matlab2019a	Mathworks	RRID:SCR_001622
HCImage	Hamamatsu Photonics	RRID:SCR_015041

RESOURCE AVAILABILITY

Lead contact

Further information and requests for code and data should be directed to the lead contact Xue Han (xuehan@bu.edu).

Materials availability

This study did not generate new unique reagents.

Data and code availability

- Data are available from lead contact upon request.
- Codes used for data analysis is available on Github repository: https://github.com/HanLabBU.
- Any additional information required to reanalyze the data reported in this paper is available from the lead contact upon request.

EXPERIMENTAL MODEL AND SUBJECT DETAILS

Primary neuron cultures

All procedures were approved by the Boston University Institutional Animal Care and Use Committee (IACUC). Primary rat cortical neuron cultures were dissociated from E18 embryos of CD® Sprague Dawley IGS rats (Charles River) and plated on coverslips coated with poly-D lysine (Millipore Sigma cat # P2636) at 0.1 mg/mL in 0.1M borate buffer (pH 8.5), and bathed with plating medium containing DMEM/F12 (Gibco cat. # 21331020) supplemented with 10% Heat Inactivated FBS (R&D systems cat. # S11150), 5% Heat Inactivated Horse Serum (Thermo Fisher Scientific cat. # 26050070), 1% Penicillin/Streptomycin (Thermo Fisher

Scientific cat. # 15140122), 397 μM L-Cysteine hydrochloride (Millipore Sigma cat. # C1276), and 2 mM L-Glutamine (Thermo Fisher Scientific cat. # 35050061). 24 hours after plating, cells were switched to a feeding medium containing NBM (Gibco cat. # 21103049) supplemented with 1% Heat Inactivated Horse Serum (Thermo Fisher Scientific cat. # 26050070), 2% NeuroCult SM1 supplement (Stemcell Technologies cat. # 05711), and 1.4% penicillin/streptomycin (Thermo Fisher Scientific cat. # 15140122) and 800 μM L-Glutamine. 11 days later, 5-fluoro-2-deoxyuridine (Millipore cat. # 343333) was added at a concentration of 4 μM to prevent glial cell overgrowth. 50% of the cell culture medium was exchanged every 3 days. Neurons were transduced with 0.25 μL of AAV9-syn-SomArchon per well in 0.25 mL of feeding media, 3-4 days after plating. Cells were imaged 14-16 days after plating, in an imaging buffer containing 145 mM NaCl, 2.5 mM KCl, 10 mM glucose, 10 mM HEPES, 2 mM $CaCl_2$, and 1 mM $MgCl_2$, pH 7.4.

Animals

All procedures were approved by the Boston University Institutional Animal Care and Use Committee (IACUC). C57BL/6 adult female mice (3-6 months old on the day of recording) were used in this study. Mice were surgically implanted with an imaging chamber and a head-plate as described previously (Piatkevich et al., 2019). AAV9-syn-SomArchon (5.9×10^{-12} genome copies (GC)/ml) was injected either through an infusion cannula attached to the window after the surgery for hippocampal recordings (50–100 nl/min, 10 min total) or injected during the surgery for visual cortical recordings (two separate injections with 100 nl/min with 3min total each).

Brain slices

Simultaneous electrophysiology and voltage imaging were performed in acute brain slice. All experimental procedures were performed in accordance with protocols approved by the Harvard Standing Committee on Animal Care following guidelines described in the US National Institutes of Health Guide for the Care and Use of Laboratory Animals. Concurrent whole-cell electrophysiology and fluorescence imaging were performed in acute mouse brain slices as described before (Piatkevich et al., 2018). Briefly, embryonic day (E) 15.5 timed-pregnant female C57BL/6 mice (Charles River) were used to carry out in utero electroporation of pCAG-SomArchon-WPRE plasmid at concentration ~1 μg/μl using round plate electrodes (CUY21 electroporator, NEPA GENE, Japan). Acute brain sections (300 μm thick) were obtained from mice at P20 – P30, using cold choline-based cutting solution consisting of (in mM): 110 choline chloride, 25 $NaHCO_3$, 2.5 KCl, 7 $MgCl_2$, 0.5 $CaCl_2$, 1.25 NaH_2PO_4, 25 glucose, 11.6 ascorbic acid, and 3.1 pyruvic acid) for brain slicing and then incubated in artificial cerebrospinal fluid (ACSF) containing (in mM) 125 NaCl, 2.5 KCl, 25 $NaHCO_3$, 2 $CaCl_2$, 1 $MgCl_2$, 1.25 NaH_2PO_4 and 11 glucose (295 mOsm/kg). Both cutting solution and ACSF were constantly bubbled with 95% O_2/5% CO_2. Individual slices were transferred to a recording chamber mounted on an upright microscope (custom-modified Olympus BX51WI, see below) and continuously superfused (2–3 ml/min) with ACSF warmed to ~32°C by passing it through a feedback-controlled in-line heater (SH-27B; Warner Instruments). Cells were visualized through a 60× water-immersion objective with either infrared differential interference contrast (DIC) optics or epifluorescence to identify GFP-positive cells. Whole-cell current-clamp recordings were obtained from GFP-positive pyramidal neurons in layer 2/3 of motor cortex, using patch pipettes (tip resistance 2.2–3.5 MΩ) pulled from borosilicate glass (G150F-3, Warner Instruments). For current-clamp recordings the pipette solution consisted of in (mM): 130 K-gluconate, 10 KCl, 4 NaCl, 10 HEPES, 4 Mg2-ATP, 0.3 Tris-GTP, 14 Tris-phosphocreatine (290 mOsm/l; pH 7.28 adjusted with KOH). SomArchon fluorescence was excited via a red laser (637 nm, 140 mW, Coherent Obis 637-140 LX), which was focused onto the back focal plane of the objective (Olympus LUMFL N 60x/ 1.10 W). Neutral density filters were used such that the power recorded after the objective was ~7 mW. The laser spot was ~25 μm in diameter at the sample plane; the resulting intensity was ~15 W/mm^2. Fluorescence was collected through the same objective, passed through a 705/100 nm emission filter, and imaged onto an EMCCD camera (Andor iXON Ultra 888) at 1,000 frames/s.

METHOD DETAILS

Simulated data theory for widefield fluorescence imaging

We consider the problem of widefield fluorescent imaging in a mouse brain in the context of imaging through scattering media within the forward scattering limit. In our model (Figure S1), an incoherent source located at plane $z = 0$ is embedded at depth $z = z_t$ inside a scattering medium, whose scattering properties are characterized by the scattering phase function $p(\hat{\mathbf{s}})$, mean scattering length l_s, and anisotropic factor $g \approx 1$. The image of the scattered light field from the source is relayed by a unit magnification 4f system

and recorded by a detector that's conjugate to the plane $z = z_s$ in the sample space. Within the scattering medium, light propagation can be characterized in terms of radiance $\mathcal{R}(z, \boldsymbol{\rho}, \hat{\mathbf{s}})$ using a simplified radiative transport equation by invoking small angle approximation (Ishimaru, 1999):

$$\frac{\partial}{\partial z}\mathcal{R}(z,\boldsymbol{\rho},\hat{\mathbf{s}}) + \hat{\mathbf{s}}\cdot\nabla\mathcal{R}(z,\boldsymbol{\rho},\hat{\mathbf{s}}) = -\frac{1}{l_s}\mathcal{R}(z,\boldsymbol{\rho},\hat{\mathbf{s}}) + \frac{1}{4\pi l_s}\int p(\hat{\mathbf{s}}-\hat{\mathbf{s}}')\mathcal{R}(z,\boldsymbol{\rho},\hat{\mathbf{s}}')\mathrm{d}^2\hat{\mathbf{s}}' \qquad \text{(Equation 1)}$$

where $(\boldsymbol{\rho}, z) = (x, y, z)$ is the 3D position vector, $\hat{\mathbf{s}} = (\theta_x, \theta_y, 0)$ is a unit direction vector parameterized by the two angles assumed to be small, where $\theta_{x,y} \approx 0$.

To solve Equation 1, it is necessary to establish a boundary condition, which, in our case, can be expressed as an isotropic emitter with intensity distribution $I_0(\boldsymbol{\rho}_0)$ located at axial position $z_0 = 0$

$$J_0(\boldsymbol{\rho}_c, \boldsymbol{\rho}_d, z_0) = \frac{1}{\kappa^2} I_0(\boldsymbol{\rho}_c)\delta(\boldsymbol{\rho}_d) \qquad \text{(Equation 2)}$$

where $\kappa = n/\lambda$, n is the refractive index, λ is the wavelength. Note that here we expressed the boundary condition in terms of mutual coherence function $J(\boldsymbol{\rho}_c, \boldsymbol{\rho}_d, z) = \langle E(\boldsymbol{\rho}_+, z)E^*(\boldsymbol{\rho}_-, z)\rangle$, where $\boldsymbol{\rho}_\pm = \boldsymbol{\rho}_c \pm \boldsymbol{\rho}_d/2$, instead of radiance $\mathcal{R}(z, \boldsymbol{\rho}, \hat{\mathbf{s}})$. This is because for an imaging system, we are more interested in the propagation of mutual coherence since it characterizes correlations of light fields between pairs of points that contribute to the final fluorescence intensity. This quantity, under paraxial limit, is related to the radiance of light field as

$$J(\boldsymbol{\rho}_c, \boldsymbol{\rho}_d, z) = \int \mathcal{R}(z, \boldsymbol{\rho}_c, \hat{\mathbf{s}})e^{i2\pi\kappa\hat{\mathbf{s}}\cdot\boldsymbol{\rho}_d}d^2\hat{\mathbf{s}} \qquad \text{(Equation 3)}$$

Equation 1 together with the boundary condition Equation 2 can be solved analytically using double Fourier transform (Ishimaru, 1999). We can therefore find the mutual coherence function at the surface of the scattering medium $z = z_t$ as

$$J_0(\boldsymbol{\rho}_{0c}, \boldsymbol{\rho}_{0d}, z_t) = \frac{e^{-H(z_t,\boldsymbol{\rho}_{0d})}}{z_t^2}\int I_0(\boldsymbol{\rho}_0)e^{-i2\pi\frac{\kappa}{z_t}(\boldsymbol{\rho}_0-\boldsymbol{\rho}_{0c})\cdot\boldsymbol{\rho}_{0d}}\mathrm{d}^2\boldsymbol{\rho}_0 \qquad \text{(Equation 4)}$$

where $H(z, \boldsymbol{\rho}) = \frac{1}{l_s}\int_0^z\left[1 - \frac{1}{4\pi}P(\kappa\boldsymbol{\rho}z'/z)\right]\mathrm{d}z'$, and $P(\boldsymbol{q}) = \int p(\boldsymbol{s})e^{i2\pi\boldsymbol{s}\cdot\boldsymbol{q}}\mathrm{d}\boldsymbol{s}$ is the Fourier transform of the scattering phase function. This light field can be further propagated through a $4f$ imaging system, resulting in the measured intensity at the detector plane as

$$I_d(\boldsymbol{\rho}_{1c}, z_s, z_t) = \iint \mathrm{CSF}\left(\boldsymbol{\rho}_{1c} - \boldsymbol{\rho}_{0c} - \frac{1}{2}\boldsymbol{\rho}_{0d}, z_s - z_t\right)\mathrm{CSF}^*\left(\boldsymbol{\rho}_{1c} - \boldsymbol{\rho}_{0c} + \frac{1}{2}\boldsymbol{\rho}_{0d}, z_s - z_t\right)J_0(\boldsymbol{\rho}_{0c}, \boldsymbol{\rho}_{0d}, z_t)d^2\boldsymbol{\rho}_{0c}d^2\boldsymbol{\rho}_{0d} \qquad \text{(Equation 5)}$$

where $\mathrm{CSF}(\boldsymbol{\rho}, z) = e^{i2\pi\kappa z}\int \mathrm{CTF}(\boldsymbol{\kappa}_\perp)e^{i2\pi\boldsymbol{\rho}\cdot\boldsymbol{\kappa}_\perp - i\pi\frac{z}{\kappa}\boldsymbol{\kappa}_\perp^2}\mathrm{d}^2\boldsymbol{\kappa}_\perp$ is the 3D coherent spread function, $\mathrm{CTF}(\boldsymbol{\kappa}_\perp) = A\left(\frac{f_0}{\kappa}\boldsymbol{\kappa}_\perp\right)$ is the in-focus coherent transfer function, $A(\boldsymbol{\xi})$ is the microscope aperture, and is the focal length of the imaging lenses (Mertz, 2019). Note that here we assumed unit magnification and refractive index of the medium $n = 1$.

From Equations 4 and 5, using the definition of optical transfer function we therefore have the 3D scattering optical transfer function (SOTF) for imaging a fluorescent object embedded in scattering media as:

$$\mathrm{SOTF}(\boldsymbol{\kappa}_d, z_s, z_t) = \frac{e^{-H\left(z_t,\frac{\kappa_d}{\kappa}z_t\right)}}{\kappa^2}\int \mathrm{CTF}\left(\boldsymbol{\kappa}_c + \frac{1}{2}\boldsymbol{\kappa}_d\right)\mathrm{CTF}^*\left(\boldsymbol{\kappa}_c - \frac{1}{2}\boldsymbol{\kappa}_d\right)e^{-i2\pi\frac{z_s}{\kappa}\boldsymbol{\kappa}_c\cdot\boldsymbol{\kappa}_d}\mathrm{d}^2\boldsymbol{\kappa}_c \qquad \text{(Equation 6)}$$

Equation 6 is the main results that we use for simulating widefield neuronal imaging, the interpretation of which is that the propagation of mutual coherence can be simply considered as free space propagation with an additional attenuation factor $e^{-H\left(z_t,\frac{\kappa_d}{\kappa}z_t\right)}$ due to scattering. Note that this result not only holds for imaging of fluorescent signals in the detection path but can also be applied to delivering illumination patterns onto a scattering sample in the excitation path (i.e., targeted illumination).

Biological tissues such as the brain are typically characterized by strong forward scattering where $g \approx 1$, where the distribution of scattering angles follows the Henyey-Greenstein phase function (Jacques, 2013):

$$p(\hat{\mathbf{s}} - \hat{\mathbf{s}}') = p(\Delta \boldsymbol{s}) = \frac{1 - g^2}{\left[(1-g)^2 + g\Delta \boldsymbol{s}^2\right]^{3/2}} \quad \text{(Equation 7)}$$

Assuming a circular microscope aperture of radius r, substituting Equation 7 into Equation 6 and using the Stokseth approximation of free space 3D optical transfer function (OTF) (Stokseth, 1969), we arrive at the analytical solution of the 3D SOTF:

$$\mathrm{SOTF}(\boldsymbol{\kappa}_\perp, z_s, z_t) = e^{-H\left(z_t, \frac{\kappa_\perp}{\kappa} z_t\right)} \mathrm{OTF}(\boldsymbol{\kappa}_\perp) \mathrm{jinc}\left[\pi z_s \Delta\kappa_\perp \frac{\boldsymbol{\kappa}_\perp}{\kappa}\left(1 - \frac{\boldsymbol{\kappa}_\perp}{\Delta\kappa_\perp}\right)\right] \quad \text{(Equation 8)}$$

where $\Delta\kappa_\perp = 2NA/\lambda$, $NA = r/f_0$ is the numerical aperture of the system, and

$$\mathrm{OTF}(\boldsymbol{\kappa}_\perp) = \frac{2}{\pi}\left[\cos^{-1}\left(\frac{\boldsymbol{\kappa}_\perp}{\Delta\kappa_\perp}\right) - \frac{\boldsymbol{\kappa}_\perp}{\Delta\kappa_\perp}\sqrt{1 - \left(\frac{\boldsymbol{\kappa}_\perp}{\Delta\kappa_\perp}\right)^2}\right] \quad \text{(Equation 9)}$$

is the in-focus free space OTF. With Equation 8, we can calculate the detected image or projected pattern simply by filtering the original object/pattern in frequency space using the corresponding SOTF.

Crosstalk simulation under different illumination conditions

Using the theoretical model developed above, we compared the background fluorescence signals generated using widefield, targeted, and holographic illumination. We estimated the reduction of background fluorescent signals from non-targeted SomArchon expressing neurons, or in other words, signal cross-contamination, with the use of targeted illumination compared to standard widefield illumination. As a start, we modeled a pair of neurons that are separated by a distance D_x laterally and D_z axially (Figures S2, S3, and S4). Each neuron was assumed to be a 15 μm diameter uniformly fluorescent spherical shell. For widefield illumination, the entire FOV was illuminated equally. For targeted illumination, only a 15 μm circular ROI was projected onto the sample centered at the location of the neuron of interest. For holographic illumination, a 15 μm diameter annulus illumination with thickness of 1–3 μm was projected onto the targeted neuron. The excited fluorescence was recorded by a camera that was focused at the center of the targeted neuron. Within the targeted ROI (indicated by the red circle in Figures S2D–I, and S3C–H), we denote the total number of detected photons from the target neuron as N_s, and the total number of detected photons from all other non-target neurons as N_b. Since both neurons were imaged onto the camera, fluorescent photons within the ROI contained both the signal N_s and background N_b. And we calculate the amount of background contamination (or crosstalk) as $C = N_b/N_s$.

In the simulation, we assumed the imaging system has unit magnification and $NA = 0.4$. The excitation and emission wavelength are $\lambda_{ex} = 637$ nm, $\lambda_{em} = 670$ nm respectively, with corresponding tissue anisotropic factor $g_{637nm} = 0.89$, $g_{670nm} = 0.90$, and mean scattering length $l_{s,637nm} = 110$ μm, $l_{s,670nm} = 119$ μm (Yaroslavsky et al., 2002). Two different scenarios for optical voltage imaging were considered, namely *in vitro* imaging in 2D neuronal cell culture and *in vivo* imaging in a mouse brain. The total excitation power for simulated targeted illumination was about 1.1% of the widefield illumination condition.

For *in vitro* imaging in cultured neurons, since it typically consists of a monolayer of cells, we therefore assumed the two neurons are at the same depth $z_t = 0$ (Figures S2A and S2B) with no tissue scattering. By varying lateral distance D_x, we plotted the amount of crosstalk induced by the non-targeted neurons in Figure S2C. Both widefield illumination and targeted illumination introduce similar amount of crosstalk, as confirmed by our *in vitro* imaging experiments. Note that in reality, these two neurons should not overlap in space and should have a separation at least $D_x = 15$ μm (although $D_x < 15$ μm is still plotted for completeness), in which case the amount of crosstalk is close to 0. Therefore, we expect very little benefit of using targeted illumination for reducing crosstalk in *in vitro* imaging. However, targeted illumination still pertains certain advantages over widefield illumination in terms of photobleaching and SBR because of the reduction of stray light and non-specific background signals.

For *in vivo* imaging in a mouse brain, we assumed that the targeted neuron was located at depth $z_t = 100$ μm (see Figures S3A and S3B) inside the tissue with scattering properties given above. The amount of crosstalk at positions with varying D_x and D_z are plotted in Figure 1C. In this case, targeted illumination results in much higher reductions in crosstalk, with most significant effects when out-of-focus ($D_z \neq 0$). Example images of

the non-targeted neuron at a defocus distance $D_z = 15$ μm with varying lateral displacement $D_x = 0$ μm, 10 μm, 20 μm are given in Figures S3C–S3H, where one can see much lower intensity from the non-targeted neuron, with the crosstalk under targeted illumination only at 70%, 62% and 5.5% of the values under widefield illumination.

Note that here our simulation only considers a pair of neurons, so the induced crosstalk values are relatively low. For *in vivo* imaging where a much higher number of neurons are labeled, the signal cross-contaminations can be introduced by hundreds or even thousands of neurons collectively. In this case, the background with widefield illumination would be more detrimental as to render the in-focus neuron visually indiscernible (see Figures 1D–1G, S6A–S6D), which could further necessitate the use of targeted illumination.

It should also be noted that our actual experiments were conducted with an objective of $NA = 0.8$, whereas in our simulation the NA was set to be 0.4 due to the limitation of small angle approximation. Higher NA will lead to faster out-of-focus blurs for both excitation and emission. Thus, under targeted illumination, when out-of-focus ($D_z \neq 0$), a larger area will be illuminated though with lower intensity. The fluorescence from out-of-focus non-targeted neurons will similarly spread over a larger area at the detector. This will essentially flatten the crosstalk curve shown in Figure 1C: at fixed $D_z \neq 0$, out-of-focus crosstalk will be reduced at small lateral displacement D_x but increased for larger D_x. However, since the fluorescent background is usually contributed by a large number of out-of-focus neurons collectively (as in Figures 1D–1G), this effect will be averaged out. In fact, for a sample with evenly distributed fluorophores, the contributions from out-of-focus background will only be determined by the fill factor of the targeted illumination mask but not the collection NA.

Membrane voltage simulation

The membrane voltage v was of Izhikevich-type and defined as follows:

$$\frac{dv}{dt} = 0.04v^2 + 5v + 140 - u + I \quad \text{(Equation 10)}$$

$$\frac{du}{dt} = a(bv - u) \quad \text{(Equation 11)}$$

$$\text{if } v \geq 30 \text{ mV, then } \begin{cases} v \leftarrow c \\ u \leftarrow u + d \end{cases} \quad \text{(Equation 12)}$$

The two coupled differential equations were numerically solved using the Euler method with 1 ms step size, modeling a 1 kHz sampling rate. For the parameters, we chose: a = 0.02, b = 0.2, c = −55 mV, d = 2 as often used (Izhikevich, 2003). The input to the neuron was composed of a fixed input current to each neuron (2.8 mV) and Gaussian current noise (standard deviation = 2 mV).

To estimate the spike SBR (see details below), we divided the spike amplitude (here defined as −50 mV–30 mV = 80 mV) by the baseline voltage fluctuations, including both the biological (dynamic) noise variance and the added measurement Gaussian white noise variance. SNR was defined as the spike amplitude divided by the added Gaussian white noise variance only.

Simulation of imaging neuronal voltage dynamics under different illumination conditions

Using the models developed above, we further simulated neural spike activities under different illumination conditions *in vivo*. For every imaged neuron, we converted the simulated membrane voltage traces (with biological noise) into fluorescent traces by setting baseline fluorescence as $F = N_s$ at −70 mV, and fluorescence change as $\Delta F/F = 30\%$ per 100 mV. Shot noise was additionally added to the measurement. We set the baseline fluorescence $N_s = 1100$ photons so that the theoretical spike SNR in absence of background and biological noise is $\Delta F/\sqrt{F} = 10$. For the signal, we assumed there was a single in-focus targeted neuron located axially at depth $z_t = 100$ μm, and laterally at $x = y = 0$ μm. For the background, we assumed that there were K non-targeted out-of-focus neurons randomly distributed within the 3D volume $x, y \in [-128\ \mu m, 128\ \mu m]$, $z_t \in [110\ \mu m, 300\ \mu m]$, with their membrane voltage dynamics assumed independent. The final simulated detected fluorescent traces were calculated from summing the fluorescent traces of all neurons (targeted and non-targeted), weighted by their respective contributions to the detected photons within the ROI. The level of background contamination was calculated as $C = N_b/N_s$ as described previously. The spike detection and spike SBR estimation algorithms were the same used for actual experiments (described below).

Custom widefield optical imaging setup

We customized a dual color widefield fluorescence microscope, which used a 470 nm LED (Thorlabs, M470L3) for GFP fluorescence excitation, and a 637 nm fiber-coupled laser (Ushio America Inc., Necsel Red-HP-FC-63x, 6 W output power) for SomArchon fluorescence excitation. The two illumination channels were combined using a dichromatic mirror (Thorlabs, DMLP550R) and subsequently directed onto the sample. The generated fluorescent signal was epi-collected by a microscope objective (Nikon, 40×/0.8NA CFI APO NIR) and imaged onto a camera (Hamamatsu, ORCA-Lightning C14120-20P) with a 175 mm tube lens. A combination of excitation filter, dichromatic mirror, and emission filter (Semrock, LF405/488/532/635-A-000) was used to separate fluorescent signals from the excitation light.

To pattern the illumination in the SomArchon imaging channel, the output of the 637 nm multimode laser was collimated (Thorlabs, F950SMA-A), expanded (Thorlabs, BE02M-A), and directed onto a DMD (Vialux, V-7000 VIS) at approximately 24° to its surface normal. The DMD was further imaged onto the sample with a 175 mm lens and the objective, so that only sample regions corresponding to the 'on' pixels of DMD were illuminated. The axial position of the DMD was adjusted so that it is conjugate to the camera, and an additional affine transform was estimated to register the pixels between the DMD and the camera. The DMD was controlled using custom Matlab script based on Vialux ALP-4.2 API.

During each imaging session, a GFP fluorescence image was first taken for illumination target identification, where a small rectangular ROI was manually selected for each individual neuron to be imaged. A binary illumination mask was then generated based on all the selected ROIs and uploaded to the DMD for illumination targeting. For widefield illumination, a single rectangular ROI that was large enough to illuminate all targeted neurons was displayed on the DMD. SomArchon voltage imaging was performed at 500 Hz, with 2 × 2 pixel binning, resulting in an imaging area of 1,152 × 576 pixels on the sCMOS camera sensor, corresponding to a 360 × 180 μm^2 FOV at the sample. To estimate sCMOS camera dark level and intrinsic noise, videos were collected with the camera set to the same acquisition parameters as during regular imaging experiments, but without light exposure (500 Hz, 2 × 2 pixel binning, 1,152 × 576 pixels imaging area). The sensor dark level was estimated to be 767.7, with an intrinsic noise of 12.6 (standard deviation) per pixel.

QUANTIFICATION AND STATISTICAL ANALYSIS

Data analysis

All imaging data were acquired by HCImage software (Hamamatsu), and further processed using MATLAB (Mathworks) offline.

Neuron ROI selection and signal analysis

All data analysis was performed offline in Matlab 2019b or 2020a. SomArchon fluorescence images were first motion corrected using a pairwise rigid motion correction algorithm as described previously (Pnevmatikakis and Giovannucci, 2017). For targeted illumination recordings, each ROI was centered on a neuron of interest, with the ROI size slightly greater than the outline of the neurons, so that motion correction can be performed on each targeted ROI that had distinguishable features identifiable by the algorithm. After motion correction, we manually selected ROIs corresponding to individual neurons, based on the average SomArchon fluorescence image during the first recorded trial. ROIs were cross-referenced by comparing SomArchon fluorescence with the stable EGFP fluorescence. The identified neurons were then applied to all subsequent trials in the same recording session. SomArchon fluorescence traces were then extracted for each neuron by averaging all the pixels within the neuron across the entire experiments. For direct comparison of SomArchon fluorescence of the same neurons between widefield and target illumination conditions, the same neuron ROIs were used for both recording conditions. Trace time segments with sharp, drastic changes in fluorescence (e.g. due to motion) were detected as outliers and excluded from further analysis in both the widefield and targeted illumination analysis. Specifically, for the outlier detection we applied the generalized extreme Studentized deviate test on the moving standard deviation values using a sliding window of ±60 ms on spike-removed traces (see STAR method Section spike detection and spike SBR calculation). In some cases, not all time points during the period of an artifact were marked as outliers. Time points between outliers (<3 data points) were therefore interpolated. To remove further artifacts, we excluded time points that were 6 standard deviations outside the trace fluorescence distribution. Time points between and around the detected outliers were also removed (±350 ms) as those periods often

coincided with extended animal motion artifacts. Occasionally, we detected small narrow band (at 80Hz) motion artifact due to air cooling ventilator system of the sCMOS camera. This artifact does not impact spike analysis but needs to be carefully considered for any subthreshold analysis.

SomArchon photobleaching estimation

To estimate the photobleaching rate of SomArchon, we first removed spikes by applying a median filter (window of 1,001 frames), and then subtracted the camera dark level (measured as 767.7). The Matlab option 'truncate' was enabled to prevent edge defects in the median filtered line. We calculated photobleaching as the rate of photodecay, as the ratio of the mean fluorescence intensity during the first 600 ms and that during the last 600 ms for each trial, and then averaged across all trials. In cultured neurons, we detected a drastic fluorescence drop within the first few seconds of recording, likely mainly due to bleaching of autofluorescence unrelated to SomArchon, thus we excluded the first two trials from subsequent analysis for culture neuron analysis.

Spike detection and spike SBR calculation

For spike detection and SBR calculation, fluorescence traces were first high-pass filtered (>16.7Hz). To separate spikes from subthreshold voltage fluctuations, we first generated a "Smoothed Trace" (ST) by averaging the fluorescence trace using a moving window of ± 100 frames. To estimate baseline fluctuation, we first removed potential spikes from the trace (T) by replacing any fluorescence values above the smoothed trace (ST) with the corresponding values of the smoothed trace ST resulting in a spike-removed trace T_{lf} (lower half trace).

$$T_{lf} = \begin{cases} T, & T<ST \\ ST, & T \geq ST \end{cases} \quad \text{(Equation 13)}$$

Similarly to T_{lf}, we constructed a trace that captures fluorescence values (T) that are likely to be spikes. In this case, T_{uf} (upper half trace) is the trace with values lower than the smoothed trace ST are replaced with ST.

$$T_{uf} = \begin{cases} ST, & T<ST \\ T, & T \geq ST \end{cases} \quad \text{(Equation 14)}$$

We then generated the derivative of T_{uf} and T_{lf} (diff_T_{uf} and diff_T_{lf}). Spikes were determined to be points where diff_T_{uf} were greater than the average (μ) of diff_T_{uf} plus the standard deviation (σ) of the diff_T_{lf} multiplied by a threshold value.

$$\text{Spikes} = \text{diff\_}T_{uf} > \mu(diff\_T_{uf}) + \sigma(diff\_T_{lf}) \times \text{threshold} \quad \text{(Equation 15)}$$

To estimate the SBR of each spike, we first obtained the spike amplitude by calculating the difference between the spike fluorescence and the lowest fluorescence value within three time points prior the spike. We then estimated the baseline fluctuation (B) as 2 times the standard deviation (σ) of the T_{ul}, since half of the fluctuations were removed in the spike removal step described above, and minus the camera intrinsic noise to obtain camera-independent estimates. The camera intrinsic noise is the standard deviation of pixel readout values with no illumination, measured as 12.6 per pixel. Finally, we calculated the SBR by dividing the spike amplitude with the baseline fluctuation.

Pearson correlation analysis

Pearson cross-correlation was performed using the Matlab functions *corrcoef* and *xcorr*, for both Vm-Vm and spike-spike correlation analysis. To calculate spike-spike correlation, spike vectors were smoothed over a ± 10 ms time window for each spike before applying correlation analysis. To calculate Vm-Vm correlation, we removed spikes by replacing 3 data point centered at each identified spike times with the adjacent values that largely eliminated the contribution of spikes in Vm-Vm correlation analysis.

Statistical analysis

In vitro recording sessions consisted of alternating trials of targeted and widefield illumination and always started with a targeted trial. To address for temporal discrepancies between the two conditions, half the neurons in each FOV were randomly assigned a sequence of trials in a recording session that either started with targeted or widefield. Equal number of targeted and widefield trials were selected for each neuron. This random assignment was performed a thousand times and the difference in SBR, spike rate,

and photobleaching between targeted and widefield trials were constructed into their respective distributions. A parameter was determined to be statistically significant if zero is above 97.5% or below 2.5% ($P < 0.05$). The boxplots in Figure 2 represent a single iteration where the difference between targeted and widefield for SBR, spike rate, and photobleaching have the same median to the corresponding one thousand random assignment distribution.

Paired student's t-tests were used for comparisons involving the same neurons between the targeted illumination condition and the widefield illumination condition. For cross correlations of *in vivo* Vm and spike-spike, half of the neuron pairs were randomly assigned to a sequence of trials starting with targeted illumination while the other half were assigned a sequence starting with widefield. Friedman's test, 2 factor non-parametric ANOVA, was used to compare the difference between the average correlations at each bin in Figure S10. Paired student's t-test was used to determine statistical significance for *in vivo* SBR, spike rate, and photobleaching.

iScience, Volume *24*

Supplemental information

Large-scale voltage imaging in behaving mice using targeted illumination

Sheng Xiao, Eric Lowet, Howard J. Gritton, Pierre Fabris, Yangyang Wang, Jack Sherman, Rebecca A. Mount, Hua-an Tseng, Heng-Ye Man, Christoph Straub, Kiryl D. Piatkevich, Edward S. Boyden, Jerome Mertz, and Xue Han

Supplementary Materials:

Supplementary Figures:

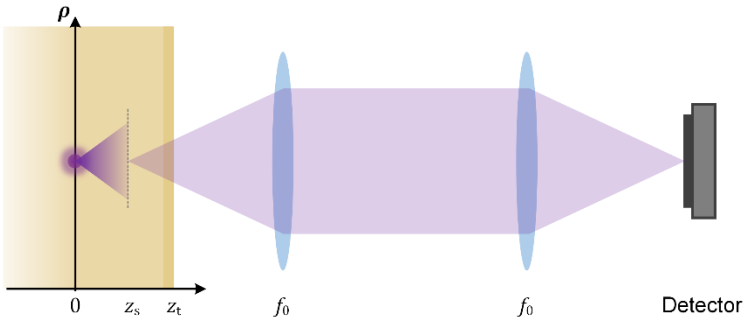

Figure S1: Theoretical model for simulating fluorescent imaging in a mouse brain, related to Figure 1. *An incoherent source located at $z = 0$ is at distance z_t away from the surface of the scattering media, z_s away from the focal plane of the microscope. The fluorescent signal is imaged by a unit magnification $4f$ system to the detector.*

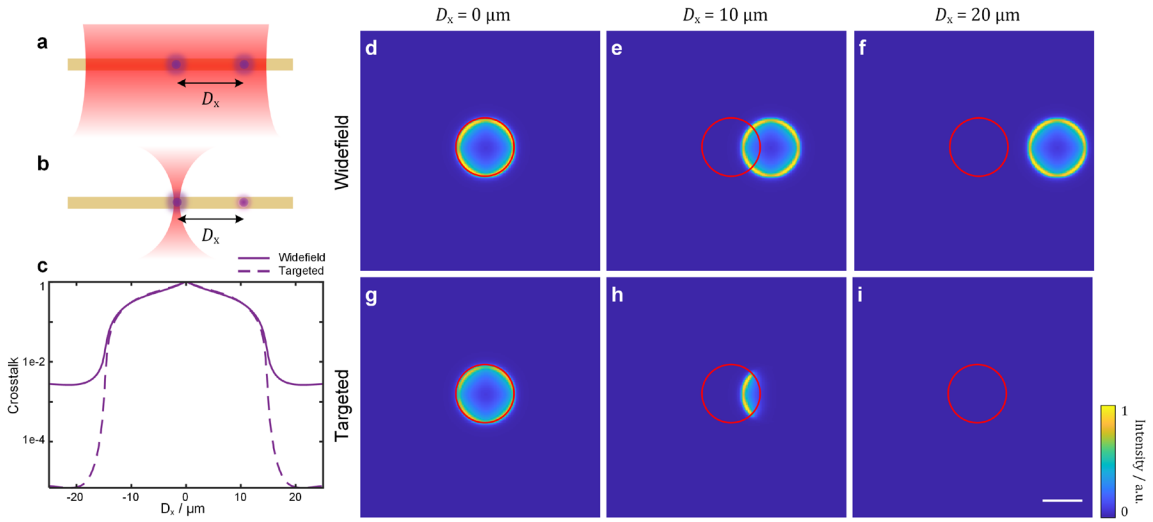

***Figure S2**: **Simulation results of in vitro optical voltage imaging in neural cell cultures, related to Figure 1.** (**a,b**) Illustration of in vitro imaging of a pair of neurons using widefield (**a**) and targeted (**b**) illumination respectively. (**c**) Comparison of signal crosstalk induced by the non-targeted neuron at varying lateral distance D_x. (**d-i**) Simulated images of the non-targeted neuron at lateral distance $D_x = 0$ µm, 10 µm and 20 µm under widefield (**d-f**) and targeted (**g-i**) illumination. Red circles represent the ROI of the targeted neuron. Scale bar, 10 µm. a.u., arbitrary unit.*

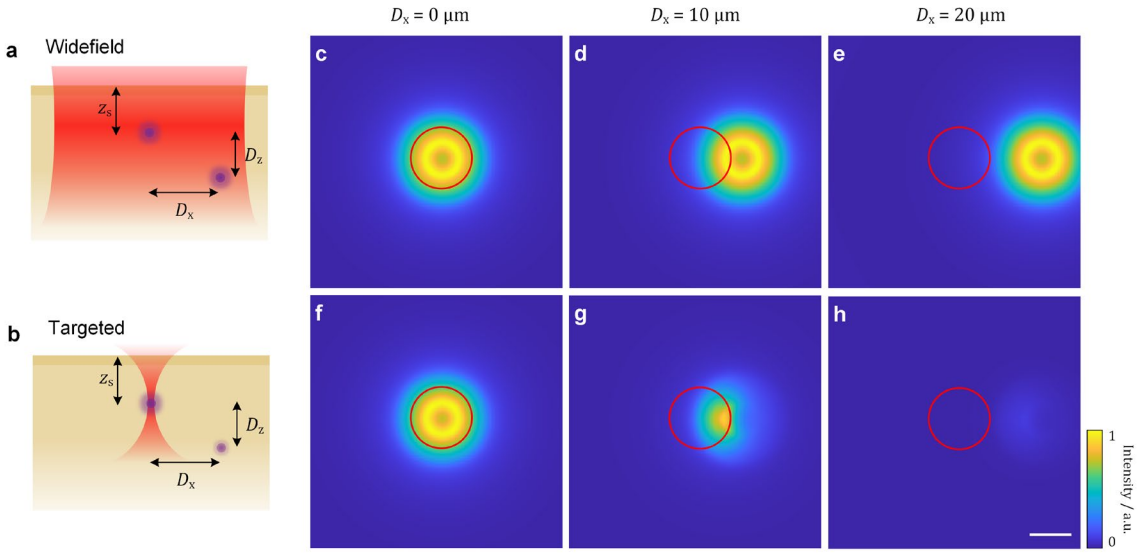

Figure S3: Simulation results of in vivo optical voltage imaging in a mouse brain, related to Figure 1. *(**a,b**) Illustration of in vivo imaging of a pair of neurons using widefield (**a**) and targeted (**b**) illumination respectively. (**c-h**) Simulated images of the non-targeted neuron at fixed axial distance $D_z = 15$ µm and varying lateral distance $D_x = 0$ µm, 10 µm and 20 µm under widefield (**c-e**) and targeted (**f-h**) illumination. Red circles represent the ROI of the targeted neuron. Scale bar, 10 µm. a.u., arbitrary unit.*

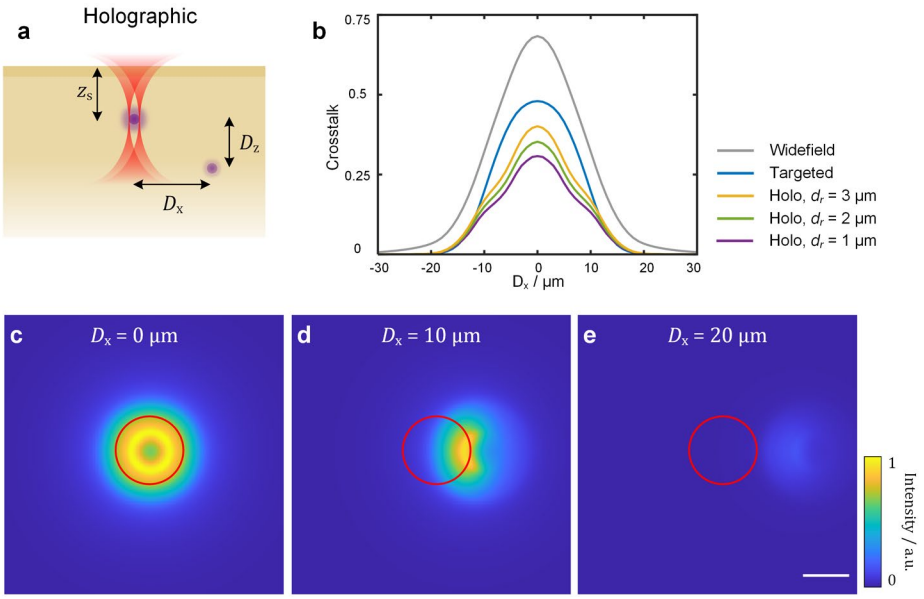

Figure S4: Comparison of holographic targeted illumination to DMD-based soma targeting and widefield illumination, related to Figure 1. *(**a**) Illustration of in vivo imaging of a pair of neurons under holographic targeted illumination where only the peripheral regions of the soma are excited. Here we assumed an annulus illumination with radius 7.5 µm and thickness d_r. (**b**) Comparison of signal crosstalk induced by the non-targeted neuron at varying lateral distance D_x and fixed defocus distance D_z = 15 µm. For holographic illumination, the amount of crosstalk additionally depends on the thickness of illumination annulus. Thinner illumination annulus leads to less crosstalk, but also reduces signal level. 3 different d_r = 1, 2, 3 µm are plotted here. (**c-e**) Simulated images of the non-targeted neuron at lateral distance D_x = 0 µm, 10 µm, 20 µm, and axial defocus D_z = 15 µm under holographic targeted illumination (d_r = 2 µm). Red circles represent the ROI of the targeted neuron. Scale bar, 10 µm. a.u., arbitrary unit.*

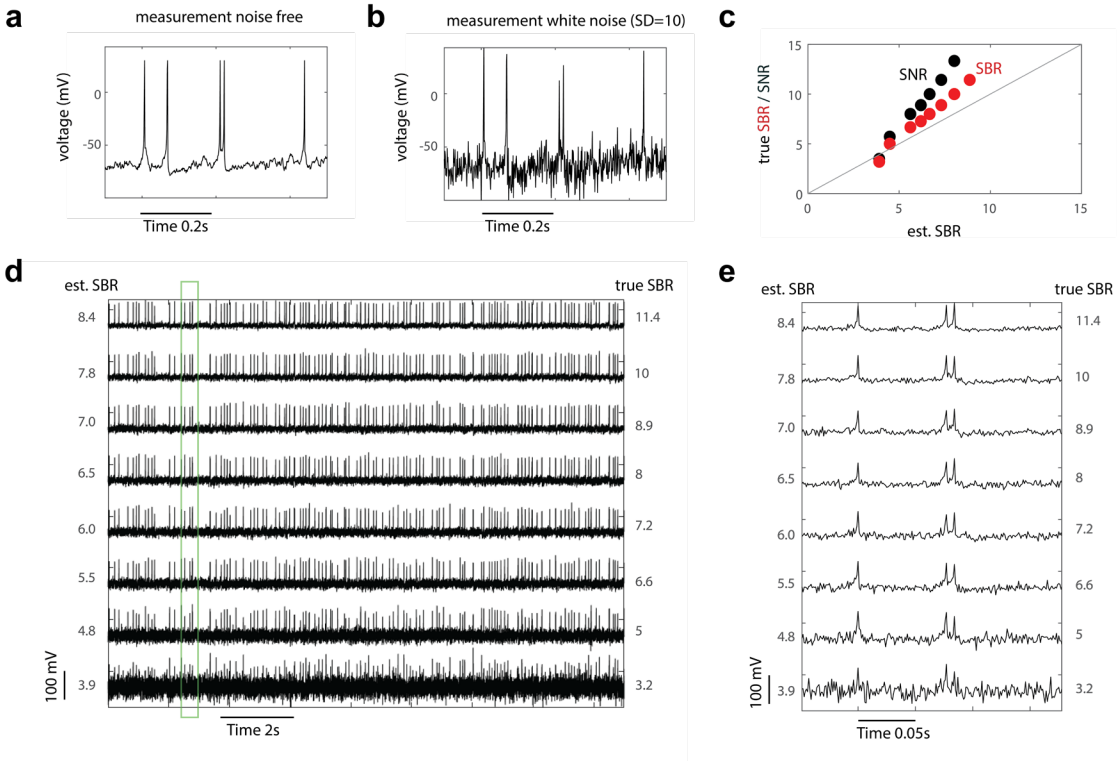

Figure S5. ***Stimulations of an integrate-and-fire neuron, with varying levels of measurement noise, related to Figure 1.*** *(**a**) Simulated membrane voltage traces without any measurement noise. (**b**) Same simulated membrane voltage trace with Gaussian white noise added (SD = 10). (**c**) Comparison of the estimated spike SBR using the same algorithm used for experimental data, and the theoretical ground truth SBR (red) and ground truth SNR (black). The ground truth SBR is defined as the spike amplitude (from base -50 mV to spike peak +30 mV = 80 mv) divided by variation of Vm that contains both the added noise and the biological noise. SNR calculation uses Vm variation containing only the added noise but not the biological noise. (**d**) The same simulated membrane voltage trace with different levels of added white noise and the corresponding estimated and ground truth SBR. (**e**) Zoomed-in version of (**d**) as indicated by the green box.*

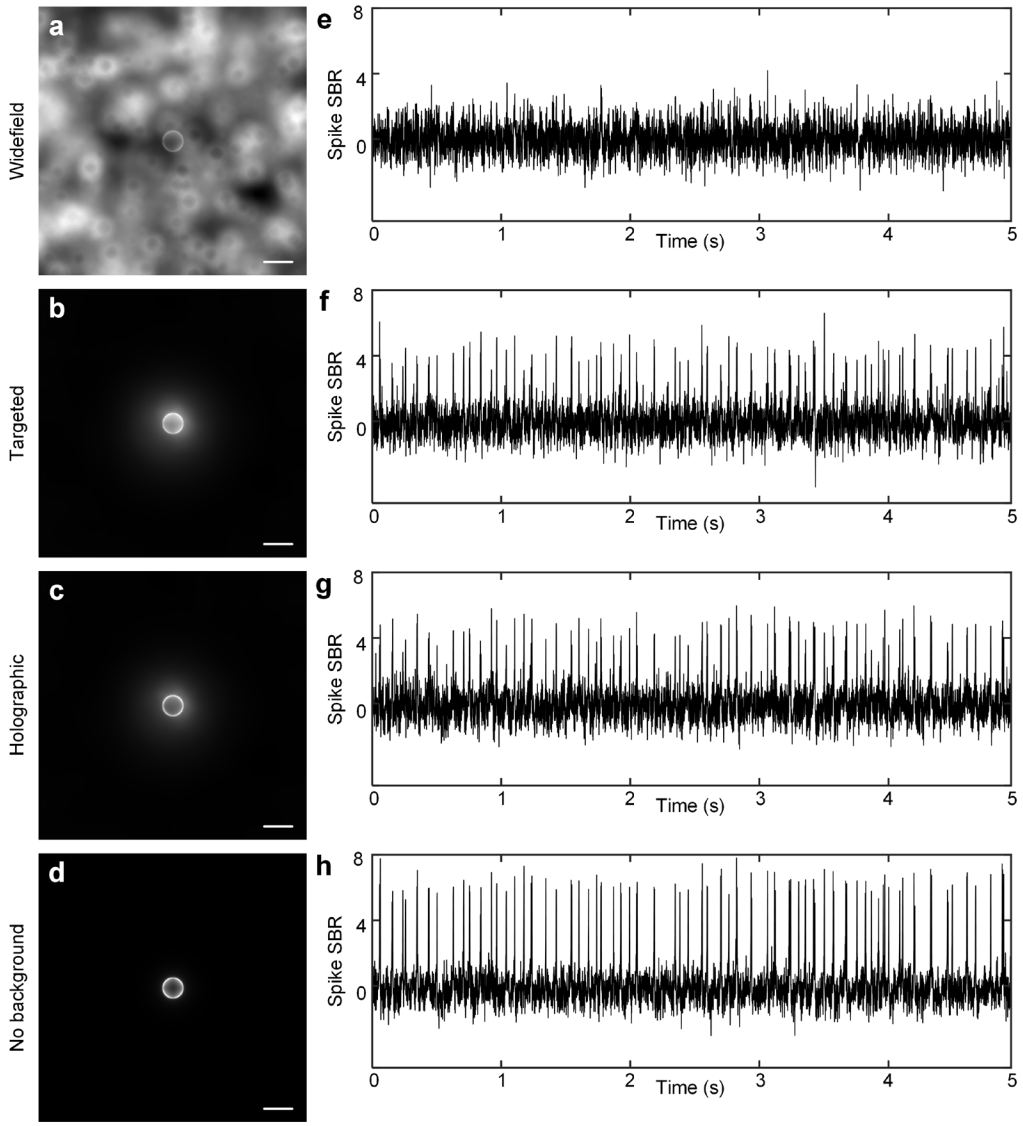

Figure S6: Simulated in vivo fluorescent voltage imaging of a single targeted neuron under different illumination conditions, related to Figure 1. *(**a-c**) Imaging of a single targeted neuron in the presence of tissue scattering and out-of-focus background under widefield, targeted, and holographic illumination. The total number of simulated out-of-focus neurons K = 5000. The measured crosstalk value $C = N_b/N_s$ from (**a-c**) are 42.2, 1.92, 1.77 respectively. (**d**) Imaging of the targeted neuron without background. (**e-h**) Simulated fluorescent traces under the conditions shown in (**a-d**) respectively. Scale bar, 20 µm.*

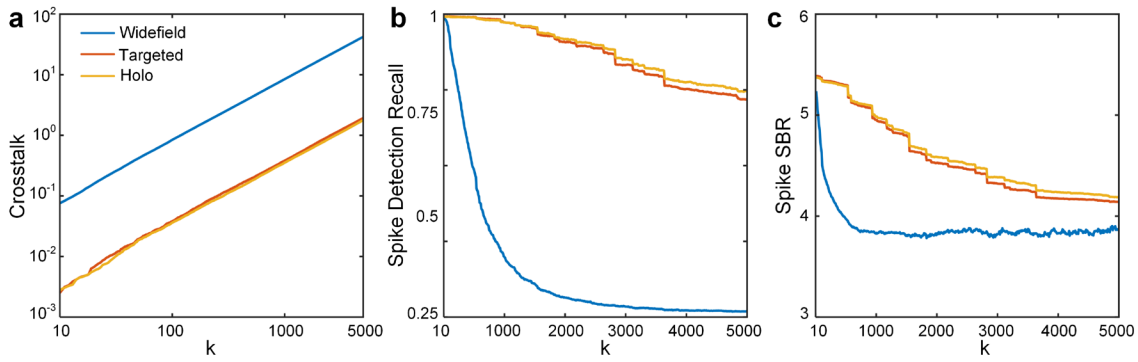

Figure S7: Statistics for simulated in vivo fluorescent voltage imaging of a single targeted neuron under different illumination conditions, related to Figure 1. *(**a**) Measured crosstalk value C as a function of out-of-focus neuron number K. (**b**) Recall of spike detection algorithm as a function of out-of-focus neuron number K. Detection threshold and other parameters were the same as used in actual experiments. (**c**) Average spike SBR for detected true positive spikes as a function of out-of-focus neuron number K.*

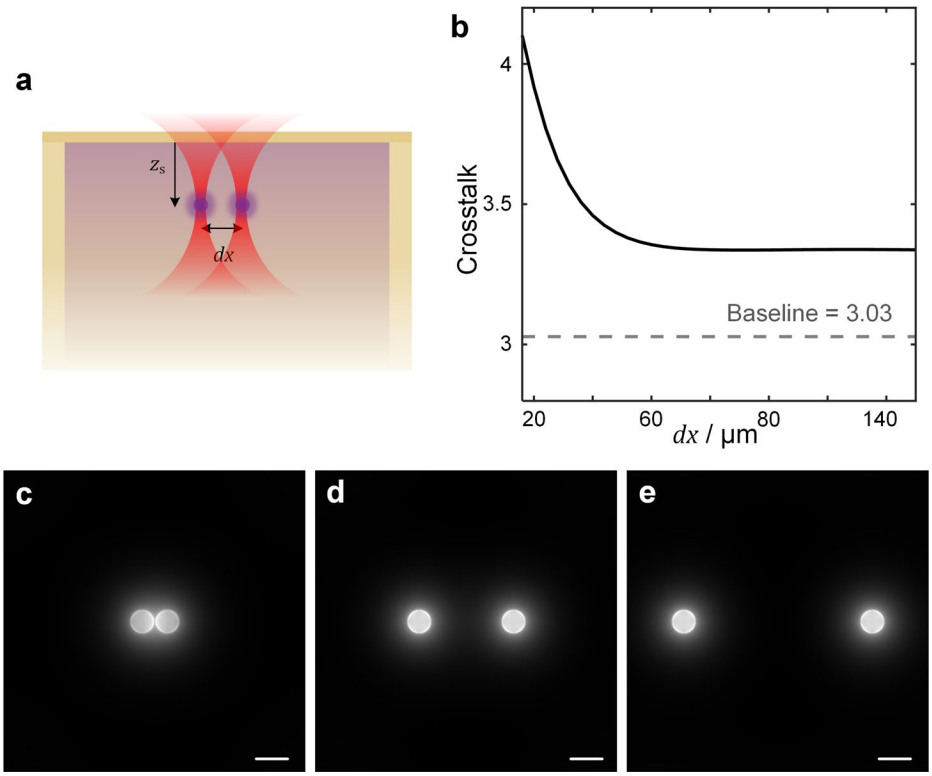

Figure S8: ***Simulation of targeted illumination imaging of two neurons in the presence of uniform background, related to Figure 1.*** *(**a**) Simulation scheme. Two neurons both located at $z_s = 100$ μm below the surface of a scattering sample, with varying center-to-center distance dx. Both neurons are targeted by the DMD excitation and are imaged onto the camera. A uniform fluorescent background is present throughout the entire sample, the concentration of which was set so that the baseline crosstalk value is 3.03 (defined as N_b/N_s when imaging a single neuron at $z_s = 100$ μm). (**b**) Measured crosstalk value for each neuron as a function of separation distance dx. As the separation distance increases, the crosstalk value reduces rapidly initially but eventually stabilizes to around 3.35. A separation distance dx near the shoulder of the curve (around 40 μm) would provide a good compromise between sampling density and induced crosstalk. (**c-e**) Example simulated images when the two neurons are separated by a distance $dx = 16, 60, 120$ μm away respectively. Scale bar, 100 μm.*

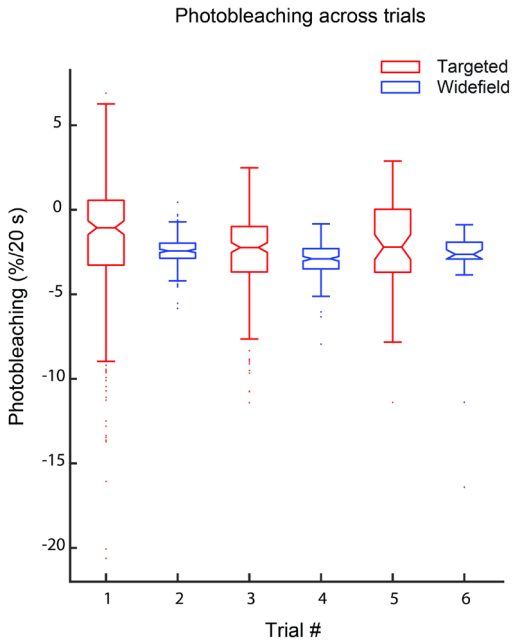

Figure S9: Photobleaching observed over alternating targeted versus widefield illumination trials in cultured neurons, related to Figure 2. *Experiments began with targeted illumination trial (trial #1), and up to 6 trials were tested across imaging sessions (n=221, 218, 216, 188, 63, and 31 neurons for trials #1-6 respectively). Each data point in the plot corresponds to the photobleaching rate obtained in each neuron on the given trial. For all boxplots, the box indicates the median (middle line), 25th percentile (Q1, bottom line), 75th percentile (Q3, top line), and the whiskers are Q1-1.5*(Q3-Q1), and Q3+1.5*(Q3-Q1). Outliers that exceed these values are shown as dots.*

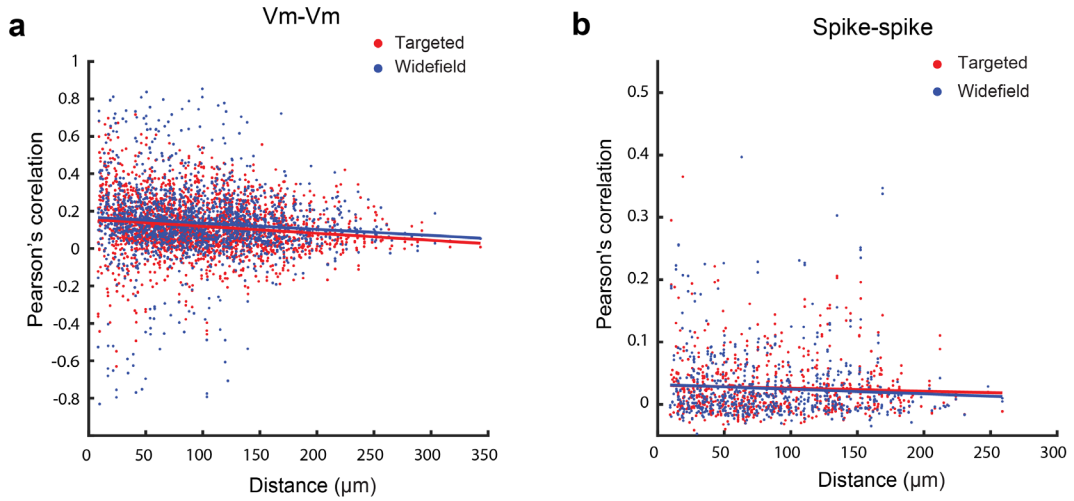

Figure S10. Effects of targeted illumination on Vm-Vm correlation and spike-spike correlation in cultured neurons, related to Figure 2. *(**a**,**b**) Pearson's correlation values between pairs of simultaneously recorded neurons decreased over anatomical distance for Vm-Vm correlation (**a**) and spike-spike correlation (**b**). Red dots indicate correlation values from pairs of neurons recorded under targeted illumination. Blue dots indicate correlation values from pairs of neurons recorded under widefield illumination.* 2 - 28 neurons were simultaneously measured in each imaging session *(14.13 ± 7.59 neurons per FOV, mean ± STD, from 16 FOVs) at 500 Hz over a FOV of* 360×180 *μm^2. Both Vm-Vm and spike-spike correlation decreased with increasing anatomical distance (slopes for linear regression of Vm-Vm correlation over distance are -3.8e^{-4} and -3.2e^{-4} for targeted and widefield illumination respectively, and spike-spike correlation over distance are -6.1e^{-5} and 9.5e^{-5} respectively. The difference in cross-correlations over distance between targeted and widefield illumination are not significant for Vm-Vm or spike-spike correlations (p = 0.4396, F-statistic=0.6, p = 0.5139, F-statistic=0.43, ANOCOVA test).*

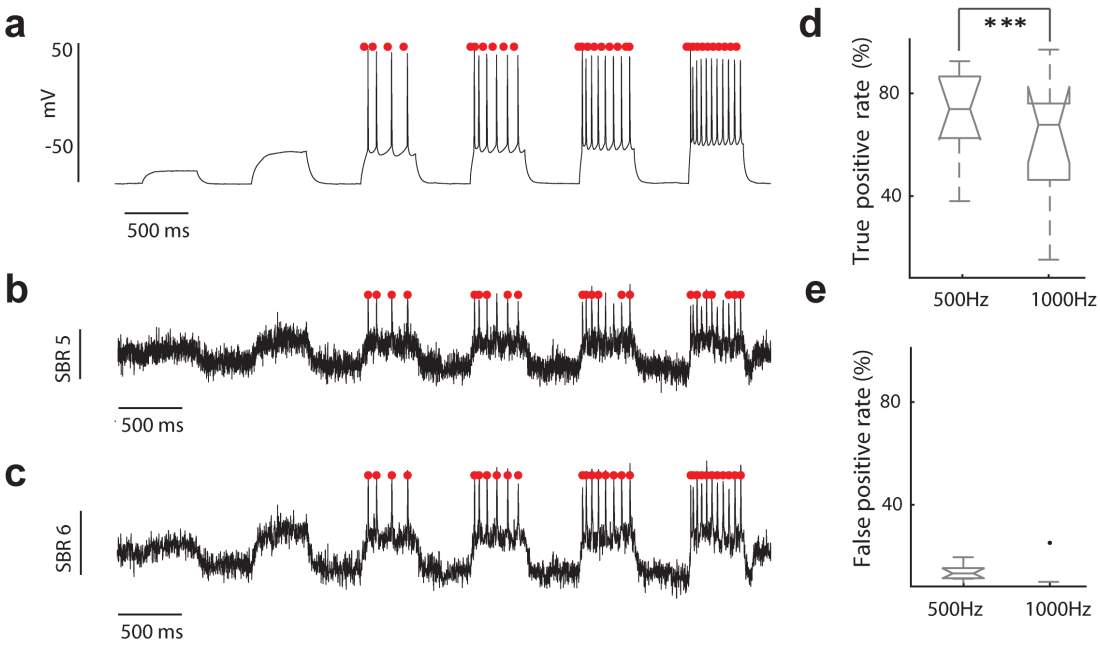

Figure S11: Spike detection rate from neurons in brain slices simultaneously recorded via patch clamp recording and SomArchon fluorescence imaging, related to Figures 2-5*. (**a-b**) An example neuron's membrane voltage trace recorded via patch clamp electrophysiology recording (**a**), and SomArchon fluorescence imaging sampled at 1000 Hz (**b**), and subsequently down-sampled to 500 Hz offline by binning consecutive frames (**c**). (**d**) True positive spike detection rates calculated as the ratio of the spikes detected in SomArchon fluorescence traces over the ground truth action potentials observed in the electrophysiology recordings (n = 10 neurons). If the spike time estimated from the SomArchon trace was within ±4 ms of the action potential peak time detected in the electrophysiology traces, it was labeled as 'detected' (true positives, 500 Hz = 72.2±5.8, 1000 Hz = 59.7% ± 7.73, mean ± STD). The true positive rate was significantly higher when SomArchon is sampled at 500 Hz than 1000 Hz ($p = 4.7324e^{-6}$, df = 9, paired t-test). (**e**) False positive spike detection rates. If the spike time estimated from the SomArchon trace was not within ±4ms of the action potential peak time detected in the electrophysiology trace, it was labeled as a false positive (500 Hz = 4.5 ± 1, 1000 Hz = 1.67% ± 1.67, mean ± STD). False positive rate was not different (p = 0.16, df = 9, paired t-test).*

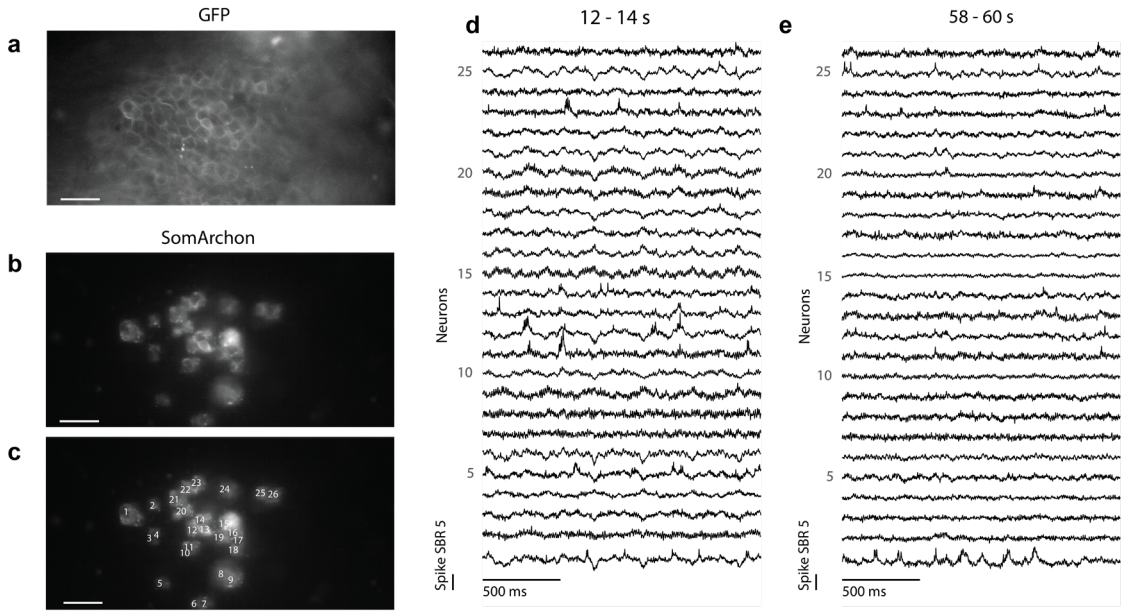

Figure S12: An example 80-second-long recording session with 25 simultaneously recorded CA1 neurons using targeted illumination in a behaving mouse, related to Figure 5. *(**a-c**) SomArchon expressing CA1 neurons in the FOV, visualized via GFP fluorescence (**a**), SomArchon fluorescence visualized with targeted illumination (**b**), and with each neuron marked (**c**). Scale bar, 50 µm. (**d,e**) Example fluorescence traces of simultaneously recorded 25 neurons. Shown are the time segments at 12-14 s (**d**) and 58-60 s (**e**) of the overall recordings.*

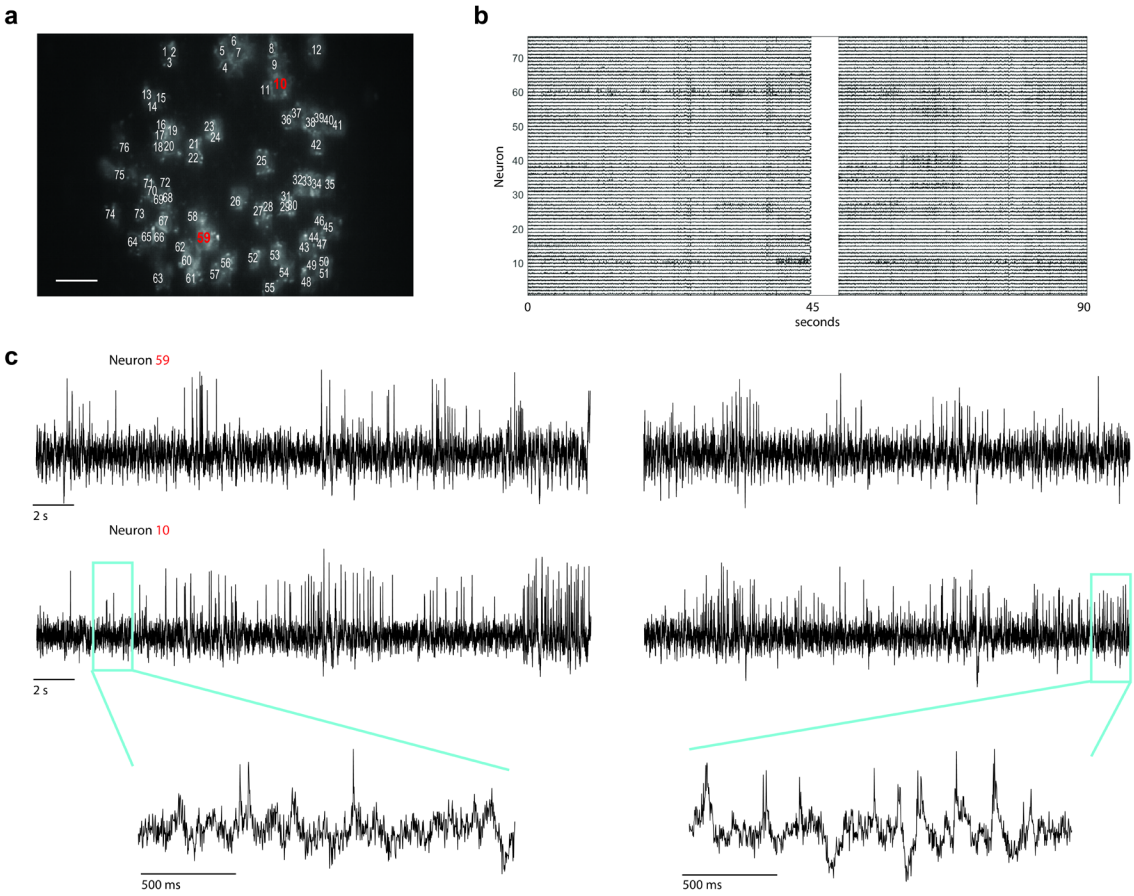

Figure S13: Fluorescent traces of the simultaneously recorded 76 CA1 neurons over the entire 90-second-long recording duration, related to Figure 5. ***(a)*** *SomArchon fluorescence visualized with targeted illumination, with each neuron marked. Scale bar, 50 µm. The two example neurons plotted in (**c**) are highlighted in red. (**b**) 90-second-long voltage traces from all 76 CA1 neurons. There was motion artifact at ~45-50 sec, which is represented by the blank period. (**c**) Whole trial traces for neurons 10 and 59. For both neurons, spikes can be detected over the entire period. Zoom in view shows the optical voltage trace of neuron 10 at the beginning and the end of the recording period.*